Palaeogeography, Palaeoclimatology, Palaeoecology 628 (2023) 111758

Contents lists available at ScienceDirect

Palaeogeography, Palaeoclimatology, Palaeoecology

journal homepage: www.elsevier.com/locate/palaeo

Hydroclimate reconstructions in the Suguta Valley, northern Kenya, during the Early-Middle Pleistocene Transition

Elena Robakiewicz [a,b,*], R. Bernhart Owen [c], Carolina Rosca [a,f], Alan Deino [d], Yannick Garcin [e,g], Martin H. Trauth [e], Simon Kübler [h], Annett Junginger [a,i,*]

[a] Department of Geosciences, Eberhard Karls University Tuebingen, Hoelderlinstr. 12, 72074 Tübingen, Germany
[b] Department of Earth Sciences, University of Connecticut, Beach Hall, 354 Mansfield Rd #207, Storrs, CT 06269, USA
[c] Hong Kong Baptist University, Department of Geography and David C. Lam East-West Institute, Kowloon Tong, Hong Kong
[d] Berkeley Geochronology Center, 2455 Ridge Road, Berkeley, CA 94709, USA
[e] Institute of Geosciences, University of Potsdam, Potsdam, Germany
[f] Instituto Andaluz de Ciencias de la Tierra (IACT), Consjeo Superior de Investigaciones Científicas, Avenida de las Palmeras 4, 18100 Armilla, Granada, Spain
[g] Aix Marseille University, CNRS, IRD, INRAE, CEREGE, Aix-en-Provence, France
[h] LMU Munich, Department of Earth and Environmental Sciences, Geology, Luisenstr. 37, 80333 Munich, Germany
[i] Senckenberg Centre for Human Evolution and Paleoenvironment (SHEP), Sigwardstrasse 10, 72072 Tübingen, Germany

ARTICLE INFO

Editor: Dr. Howard Falcon-Lang

Keywords:
Suguta-Turkana-Baringo Basin
Paleolimnology
Geochemistry
Diatom
Tephra
Quaternary

ABSTRACT

The Early-Middle Pleistocene Transition (EMPT) between 1200 and 700 ka represents a major global climate transition from dominantly 41,000- to 100,000-year glacial cycles. The forces and mechanisms behind this transition and the response of African environments are not well understood. The active volcanism and tectonics of the East African Rift System add complexity to local environmental systems and can erase important proxy records, inhibiting studies of lacustrine dynamics. As a result, there is minimal understanding of how this transition impacted the region's lake systems. At Paleolake Suguta, in the northern Kenya Rift, however, flood basalts cap lacustrine EMPT-age deposits, preserving these strata and their valuable paleoenvironmental record. This research presents a high-resolution reconstruction of hydrological change from approximately 931 to 831 ka within the Suguta-Turkana Basin in the northern Kenya Rift. Paleolake dynamics are reconstructed from a 41 m sedimentary section using diatom morphology, sedimentology, and X-Ray Fluorescence elemental analysis. Results show that lake levels varied greatly during this part of the EMPT with two wetter phases and two drier phases developing over about 100 kyr. From ~885–831 ka, especially, the Suguta-Turkana Basin exhibits rapid changes in paleohydrology, ranging between deep stratified lakes; shallow, well-mixed lakes; and complete desiccation, with some of these changes occurring on an order of hundreds of years. This EMPT Suguta-Turkana-Baringo record therefore provides valuable insight into hydroclimate variability at an overall resolution of several thousand years, allowing reconstruction of past environments during a period of poorly understood terrestrial environmental change.

1. Introduction

One of the most pronounced global climate changes of the Quaternary, the Early-Middle Pleistocene Transition (EMPT), occurred between 1200 and 700 ka. During the EMPT, glacial-interglacial cycles became longer and more intense, changing from 41- to 100-kyr cycles (e.g., Shackleton and Opdyke, 1977; Pisias and Moore, 1981; Mudelsee and Stattegger, 1997), possibly a result of long-term cooling trends associated with changing pCO_2 and thickening of Northern Hemisphere ice sheets (e.g., Mudelsee and Schulz, 1997; Maslin and Ridgwell, 2005; Clark et al., 2006; Head et al., 2008; Maslin and Brierley, 2015). This intensification led to abrupt "saw-toothed" glacial-interglacial transitions via two stages (Maslin and Brierley, 2015). The first (900–700 ka) resulted in a significant increase in global ice volume over 41-kyr cycles (Mudelsee and Stattegger, 1997; Maslin and Brierley, 2015), after which (post-700 ka), the climate system became a more complex three-state system with full interglacials, full glacials, and intermediate interglacials over 100-kyr cycles (Paillard, 1998).

* Corresponding authors at: Department of Geosciences, Eberhard Karls University Tuebingen, Hoelderlinstr. 12, 72074 Tuebingen, Germany.
E-mail addresses: elena.robakiewicz@uconn.edu, elena.robakiewicz@ifg.uni-tuebingen.de (E. Robakiewicz), annett.junginger@uni-tuebingen.de (A. Junginger).

https://doi.org/10.1016/j.palaeo.2023.111758
Received 9 May 2023; Received in revised form 2 August 2023; Accepted 2 August 2023
Available online 4 August 2023

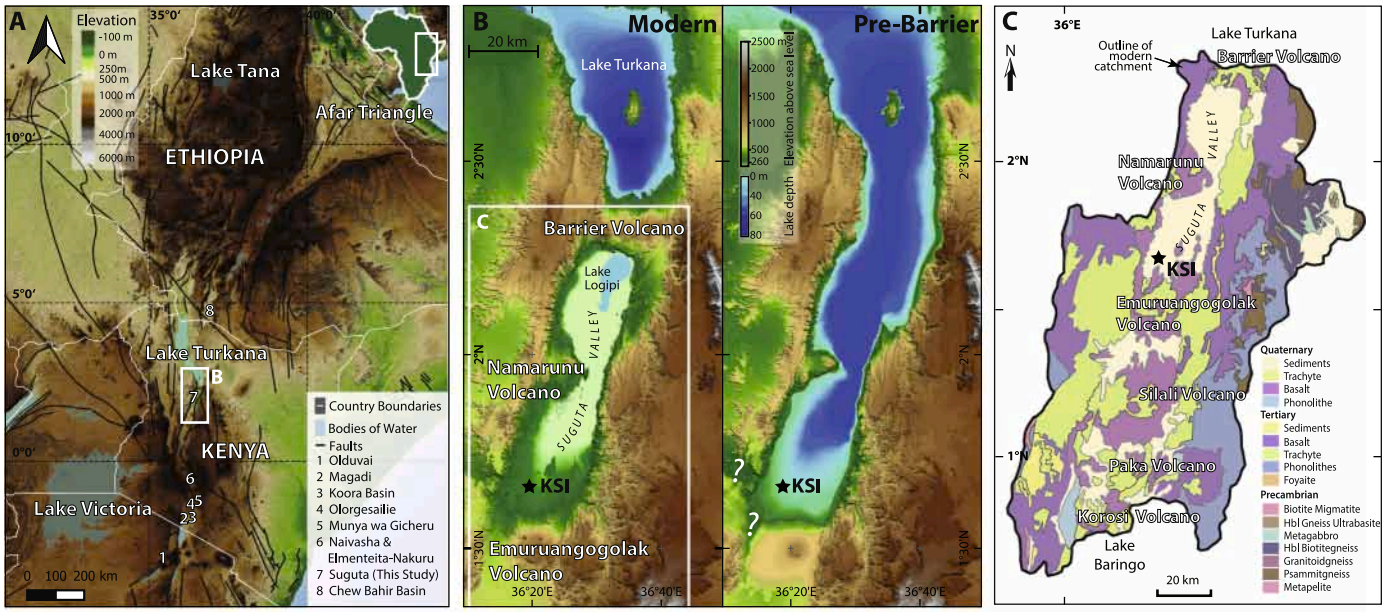

Fig. 1. **(A)** Map of the Eastern Branch of the East African Rift System (EARS) including elevation, large bodies of water, and faults. Sites included in this study are also shown from south to north: **1** Olduvai (Stanistreet et al., 2020); **2** Lake Magadi (Owen et al., 2018a; 2019) **3** Koora Basin (Deino et al., 2019a); **4** Olorgesailie (Owen et al., 2014; Potts et al., 2018); **5** Munya wa Gicheru (Owen et al., 2014); **6** Naivasha and Elmenteita-Nakuru (Trauth et al., 2007); and **7** Paleolake Suguta (This Study). The study area is highlighted with a white box. **(B)** Modern versus Pre-Barrier Volcanic Complex topographic maps showing the change between the Suguta and Turkana basins including the uncertainty in the topography in the southern portion of the basin Pre-Barrier Volcanic Complex. The location of the geological map in C is outlined. **(C)** Geological map of the modern Suguta catchment. The studied outcrop, KSI, is starred. Sources for this map include Baker (1963), Dodson (1963), Makinouchi et al. (1984), Ochieng (1988), Van Kekem (1986), Mosley (1993), and Ackermann and Heinrichs (2001).

Eastern African hydroclimate responds to a combination of local tectonic processes (Xue et al., 2019), global temperatures/pCO_2, low-latitude insolation forcing (Clement et al., 2004; Deino et al., 2006; Trauth et al., 2009; Joordens et al., 2011; Yost et al., 2021), tropical sea surface temperatures (Vuille et al., 2005; Tierney et al., 2011; Johnson et al., 2016), and glacial-interglacial cycles (Larrasoaña et al., 2003; Rossignol-Strick, 1984; Kutzbach et al., 2020). The relative strength and importance of each factor through time remains largely unknown and variable (Lupien et al., 2022), resulting in uncertainty over how regional environments responded to the EMPT. Fortunately, within the Suguta Valley in the northern Kenya Rift (36.55°E, 2.22°N), flood basalts have capped lacustrine sediments of this age (Dunkley et al., 1993), preserving them and enabling an examination of regional hydroclimate.

This study fills a gap in northern Kenya Rift sedimentological records between 900 and 700 ka and helps increase understanding of EMPT paleoclimatology and paleoenvironments. Previous studies in the neighboring Turkana Basin indicate that a floodplain dominated, with erosion and/or non-deposition to the northeast and south (Feibel, 2011). Brown and McDougall (2011) noted a paucity of sedimentary evidence between 1000 and 800 ka and an absence of ~700–200 ka strata, although studies at neighboring Chew Bahir provide a record back to 620 ka (Duesing et al., 2021; Foerster et al., 2022). Similarly, the southern Baringo Basin indicates a ~ 1 Myr unconformity between the end of the Chemeron Formation (~1570 ka Hill et al., 1986) and the beginning of the Kapthurin Formation (~610 ka Deino and McBrearty, 2002) with many lacustrine phases of the Kapthurin Formation indicating alkaline and saline lakes (Renaut et al., 1999). Here, we present a new hydroclimate dataset from a lacustrine sequence (KSI) deposited between ~931 and 831 ka, coinciding with a paucity of sedimentary evidence at Turkana and other East African Rift System (EARS) basins. This study aims to explore EMPT hydroclimate variability within the Suguta-Turkana-Baringo Basin and understand its regional impacts.

2. Setting

2.1. Geological setting

The Suguta Valley (northern Kenya Rift) forms part of the eastern branch of the EARS, a 3000-km-long continental rift initiated during the Miocene by mantle plume activity (Fig. 1A: Ebinger and Sleep, 1998; Ebinger et al., 2000; Chorowicz, 2005; Pik et al., 2008; Purcell, 2018). Initial uplift and doming gave way to north-south Plio-Pleistocene rifting (Baker and Wohlenberg, 1971) forming the Suguta Valley due to subsidence along the inner trough by at least ~1.8 Ma, with coeval volcanism separating it from other basins (Morley et al., 1992; Dunkley et al., 1993). In the north, the Barrier volcanic complex erupted ~1.37 Ma and separates Suguta from Lake Turkana today, although hydrological separation was not achieved until ~221 ka (Dunkley et al., 1993; McDougall et al., 2012), a date which may be pushed back to ~780 ka (Fig. 1B: Junginger et al., 2023). To the south, the Korosi volcanic shield did not form until ~380 ka (Dunkley et al., 1993), far later than the timeframe of this study. Consequently, this study reflects changes in a larger Suguta-Turkana-Baringo catchment.

Today, the Suguta Valley is ~80 km long by 17–21 km wide (Fig. 1C), with a 12800 km^2 catchment (~180 km north-south; ~35–70 km east-west) (Dunkley et al., 1993; Garcin et al., 2009; Junginger and Trauth, 2013). The modern Suguta is a NNE-trending half graben with its floor ~1000–275 m above sea level (asl) (Bosworth and Maurin, 1993; Saneyoshi et al., 2006; Melnick et al., 2012; Junginger et al., 2014). The rift margins are faulted monoclines with a possible border fault to the northeast and hills rising to 750 (west) and 1100 m asl (east) (Dunkley et al., 1993). Basin subsidence is controlled by extensional faulting overprinted by strike-slip and compressional deformation (Dunkley et al., 1993; Le Gall et al., 2005; Vetel and Le Gall, 2006). The catchment includes Plio-Pleistocene alkaline basalts and trachytes with

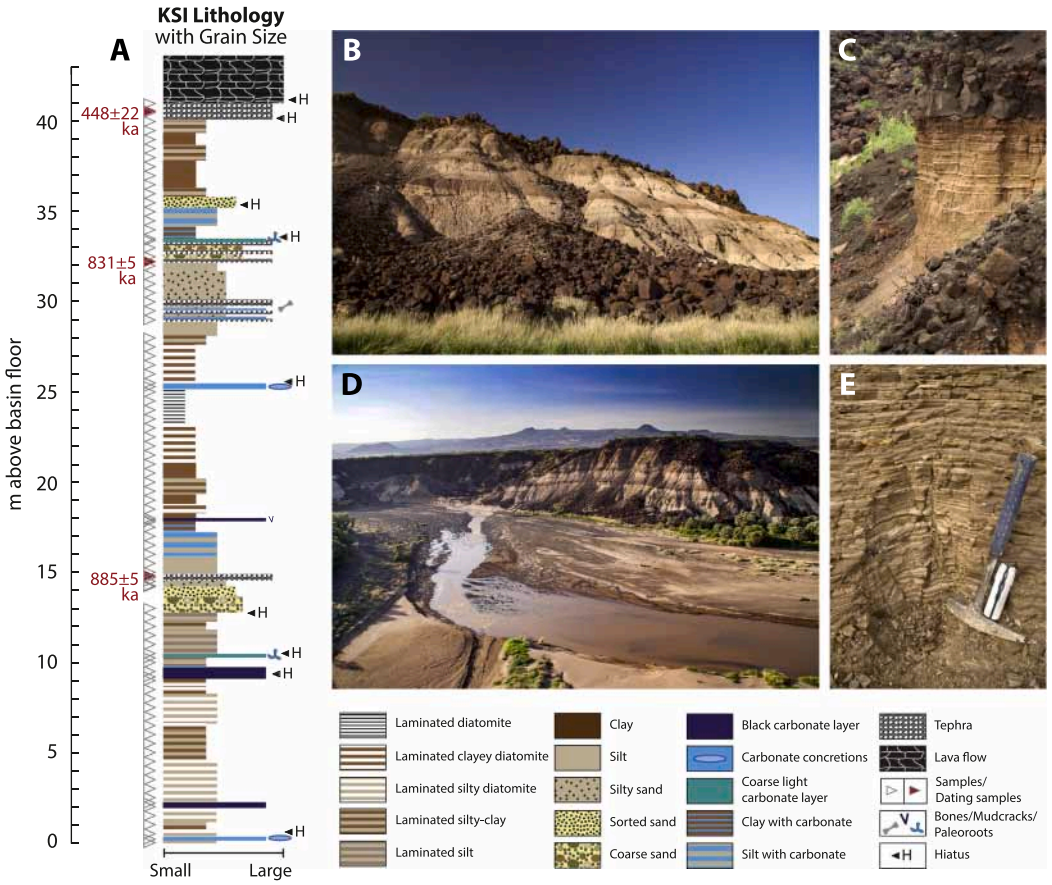

Fig. 2. **(A)** Lithographic column measured from the basin floor upwards including relative grain sizes, sample locations, and dated units of site Kamuge-Suguta I (KSI). **(B)** KSI from the base of the sequence. **(C)** Close-up of laminated sediments located underneath flood basalts at 41.2 m. **(D)** Aerial photo of KSI and the Suguta River. **(E)** Close-up of laminated diatomites located lower in the section.

Precambrian gneisses of the Mozambique Orogenic Belt in the northeast (Fig. 1B; Bosworth and Maurin, 1993; Dunkley et al., 1993).

2.2. Hydroclimatological setting

Equatorial Eastern African climate is primarily characterized by changes in precipitation rather than temperature. Rainfall is bimodal, peaking from March–May (long rains) and October–November (short rains) (Nicholson, 1996, 2017). Modern Suguta is the most arid setting in Kenya (Ojany and Ogendo, 1973), with daily temperatures of 30–50 °C; annual precipitation of <300 mm/yr, increasing to 1000 mm/yr along rift shoulders (Junginger and Trauth, 2013); and evaporation rates of 3000–4000 mm/yr (Nyenzi et al., 1981; Garcin et al., 2009). Lake Logipi, in the lowest part of Suguta, varies seasonally in response to inflows from the Suguta River, smaller ephemeral rivers, springs, and groundwater from Lakes Turkana and Baringo (Dunkley et al., 1993; Junginger and Trauth, 2013). Much of the lake desiccates into salt pans during the dry season, but, at its maximum, can cover 80 km^2 (Castanier et al., 1993). Contrasts between increased precipitation at higher elevations and hyper-arid conditions at lower elevations characterize Paleolake Suguta as an “amplifier lake”, which responds sensitively to even minor climatic changes (Olaka et al., 2010; Trauth et al., 2010).

Today’s hyper-aridity contrasts with the 300-m-deep paleolake that formed 15–5 ka during the African Humid Period (AHP) (Garcin et al., 2009; Junginger and Trauth, 2013; Junginger et al., 2014). During the AHP, precipitation is estimated to have been only 20–30% higher than today (Borchardt and Trauth, 2012; Junginger and Trauth, 2013), yet Paleolake Suguta was 75 times deeper (Garcin et al., 2009). Towards the end of the AHP, the water level of Paleolake Suguta dropped by 240 m 8.5–7.3 ka, underlining its climate sensitivity (Garcin et al., 2009).

Truckle (1976) and Dunkley et al. (1993) described Pleistocene and Holocene fluvio-lacustrine deposits as the ‘Suguta Beds’. Early to Middle Pleistocene lacustrine sediments in southern and western Suguta, between the Namarunu and Emuruangogolak volcanoes, document past humid conditions (Truckle, 1976; Casanova et al., 1988; Sturchio et al., 1993; Trauth et al., 2007). The 41-m section, Kamuge-Suguta I (KSI), northwest of Emuruangogolak, is one of the best exposed Pleistocene lacustrine sequences in the area (Fig. 1C). KSI is located along the eastern banks of the Suguta River near its confluence with the Kamuge River (1.640098°N, 36.294669°E, 362 m asl). The sediments, mostly clays, silts, and diatomites, are intercalated with carbonates and tephras and document hydroclimatic changes during part of the EMPT (Fig. 2).

3. Materials and methods

3.1. Sample collection, stratigraphy and grain sizes

Sediments were collected in 2007 from a 41-m section sampled at 50-cm intervals with additional samples taken where carbonates were present, yielding 93 samples. Grain sizes were described in the field with fine-grained lithologies also analyzed on a Malvern MasterSizer 2000 at

Eberhard Karls Universität Tübingen. Preparation followed Meyer et al. (2020) with replicate analyses (5×) to calculate 90% confidence intervals. MasterSizer results reflect both clastic grains and biogenic diatoms – a common occurrence in African sediments (Meyer et al., 2020) – limiting its interpretability. Because of these complications, the MasterSizer's results were supplemented with qualitative observations to generate the KSI stratigraphic column.

3.2. Chronology

Three KSI tuff samples consisting of coarse ash from Plinian fallout and reworked lapilli tuffs were dated by the $^{40}Ar/^{39}Ar$ method at the Berkeley Geochronology Center (BGC). Feldspar phenocrysts were separated using conventional techniques including disaggregation using a ceramic mortar and pestle, sieving, dilute HF and distilled water rinses, and hand-picking under a binocular microscope to obtain a finished product of clean grains as free of inclusions as possible.

The final mineral separates were irradiated in the Cd-lined CLICIT position of the Oregon State University TRIGA reactor for two hours (BGC irradiation #375). This irradiation employed sanidine phenocrysts from the Alder Creek Rhyolite of California (orbitally referenced age = 1.1848 ± 0.0006 Ma; Niespolo et al., 2017) as the neutron fluence monitor mineral. Standards and unknowns were co-irradiated in circular concentric rings in wells in an aluminum disk with both unknowns on the same disk. The appropriate neutron fluence factor (the '*J*' parameter of $^{40}Ar/^{39}Ar$ dating calculations; McDougall and Harrison, 1999) for the sample positions was calculated from a planar fit of the standard calibrations, with median 1σ errors derived by Monte Carlo simulation in the predicted *J* value of ~0.4%. Reactor-induced isotopic production ratios for these irradiations were: $(^{36}Ar/^{37}Ar)_{Ca} = 3.65 \pm 0.02 \times 10^{-4}$, $(^{38}Ar/^{37}Ar)_{Ca} = 1.96 \pm 0.08 \times 10^{-5}$, $(^{39}Ar/^{37}Ar)_{Ca} = 6.95 \pm 0.09 \times 10^{-4}$, $(^{37}Ar/^{39}Ar)_{K} = 3.24 \pm 0.16 \times 10^{-4}$, $(^{38}Ar/^{39}Ar)_{K} = 1.220 \pm 0.003 \times 10^{-2}$, $(^{40}Ar/^{39}Ar)_{K} = 3.5 \pm 0.9 \times 10^{-4}$. Atmospheric $^{40}Ar/^{36}Ar$ = 298.56 ± 0.31 (Lee et al., 2006) and decay constants follow (Min et al., 2000).

The irradiated sanidine phenocrysts were then analyzed at the BGC using the single-crystal $^{40}Ar/^{39}Ar$ total-fusion (SCTF) technique. Individual grains were heated rapidly to fusion and degassed in <10 s under ultra-high vacuum for several minutes. Argon measurements were carried out using an automated extraction line feeding a single-collector MAP-215 mass spectrometer, using analog multiplier signal measurement.

Age distributions obtained from a suite of SCTF analyses are often complicated by anomalous or imprecise results which were eliminated from the study, due to detrital contamination, excess ^{40}Ar trapped in primary phenocrysts, subtle alteration, potassium-poor composition, or analytical failure. Plagioclase grains (Ca/K > 2 as determined by the $^{40}Ar/^{39}Ar$ measurement process) were omitted as they exhibit much greater analytical uncertainty than the anorthoclase or sanidine phenocrysts that dominate these samples. Analyses with anomalously high analytical uncertainty, likely from incomplete fusion, fusion of non-feldspathic grains, or very small grain size (i.e., less than a few hundred microns) were also omitted. We identified distinctly older grains (xenocrysts) using a gap-finding technique (Deino et al., 2019a, 2019b), with the sensitivity set to a gap score of seven, to identify most old outliers. Lastly, we further eliminated older modes of clearly multimodal distribution that were not identified by the gap-finding routine due to proximity to the primary mode. Ultimately, the $^{40}Ar/^{39}Ar$ result is reported as the weighted-mean age of the accepted analyses, with ±1 s modified standard error, computed as the standard error expanded by the root of the mean square weighted deviation (MSWD), if MSWD >1.

We also analyzed the argon systematics using 'inverse isochron' regressions ($^{36}Ar/^{40}Ar$ vs. $^{39}Ar/^{40}Ar$) calculated from the accepted grain analyses. The age and error estimates derived from the isochron regressions are then compared to analytical weighted means.

3.3. Diatom sample preparation and counting

About 0.1 g of sample was added to 20 ml of 30% H_2O_2 and heated to 90 °C to remove organics (Battarbee, 1986). 10% HCl (to remove carbonates) and a *Lycopodium* microspore (to measure concentrations) were then added, with samples rinsed in DI water and centrifuged to remove remaining acids. Ammonia solution (30–33% NH_3) was added to separate aggregates and remove clays before a final rinsing in DI water. Samples were added to coverslips and dried for 24 h. Naphrax was used to adhere cover slips to glass slides and heated at 125 °C until cured.

When possible, at least 400 diatom valves were counted on a Fisher B2-Series light microscope at 1000× magnification. If one species was dominant, a minimum of 100 non-dominant valves were counted. Identification was conducted using Spaulding et al. (2022), Gasse (1986), Cocquyt (1998), and Taylor et al. (2007). A valve was counted if >50% of the valve was visible and identifiable. In all cases, specimens were identified to the lowest taxonomic level possible. Identifications were confirmed on a Phenom XL Scanning Electron Microscope with a Cerium Hexaborit (CeB6) cathode at the Universität Tübingen. Samples were coated with 70 nm gold and analyzed at 15 kV acceleration voltage.

3.4. Diatom analysis

Diatom concentrations were calculated using *Lycopodium* spores (Batch-050220211; 18,400 spores).

$$DiatomConcentration = \frac{(\#ofMicrospheresIntroduced^{*}\#ofCountedDiatoms)}{(1 + \#ofMicrospheresCounted)}$$

An adapted Planktonic Diatom Index (PDI) was used to characterize deep lakes (Deino et al., 2006; Kingston et al., 2007) where deep lake conditions occur when PDI ≥ 10.

$$PDI = \sqrt{\frac{\%ofPlanktonicDiatoms}{(\%ofLittoralPlanktonic + \%ofLittoralDiatoms)}}$$

Ecological interpretations are based on modern assemblage data from the East African Diatom Database within the European Diatom Database Index (EDDI) (Battarbee et al., 2001). Hydrochemical parameters (conductivity and pH) were determined using weighted averaging (ter Braak and Looman, 1986; Gasse et al., 1995). The modern African training set includes each taxon's optimum and tolerance for each environmental parameter. Paleoenvironmental parameters are estimated using the total sum of the relative percentage of each fossil taxon, weighted by its optimum, and standardized to the total percentage of the diatom assemblage used in the transfer function (Chalié and Gasse, 2002). Weighted tolerances were then added to create a range for the calculated parameter. Statistical analyses were conducted in R and are accessible in GitLab. Stratigraphic plots were made using the R package Rioja (Juggins, 2022).

3.5. XRF and PCA

Bulk samples selected for major oxide- (SiO_2, Al_2O_3, Fe_2O_3, CaO, MgO, K_2O, Na_2O, TiO_2, MnO, P_2O_5) and trace element (Ca, Cr, Ga, Nb, Ni, Rb, Sr, V, Y, Zn, Zr) analyses via X-Ray Fluorescence (XRF) were pulverized and mixed with 7.5 g MERCK spectromelt A12, followed by gradual melting up to 1200 °C to fused beads using an Oxiflux system. Measurements were carried out on a Bruker AXS S4 Pioneer XRF device (Rh-tube, 4 kW) at the Universität Potsdam.

The oxide for each sample was normalized by dividing each oxide's percentage by the total percentages without Loss on Ignition (LOI) and multiplying by 100. Samples were then converted to elemental weight percentages and parts per million (ppm).

$$Weight\%ofElement = NormalizedWeight\%ofOxide*\left(\frac{\#ofCationsinOxide*AtomicMassofCation}{AtomicMassofOxide}\right)$$

The Chemical Index of Alteration (CIA) (Nesbitt and Young, 1982) was calculated to indicate the degree of weathering of source rocks to the sediments. Numbers closer to 100 indicate more heavily weathered deposits and/or slower erosion rates (Owen et al., 2014, 2018b). To use this index, XRF data was converted into molar proportions:

$$MolarProportionoftheOxide = \left(\frac{NormalizedWeightPercentageofOxide}{MolarMassofOxide}\right)$$

The CIA was then calculated using:

$$CIA = \frac{Al_2O_3}{(Al_2O_3 + CaO^* + Na_2O + K_2O)}*100$$

CaO* (inorganic CaO) was estimated by subtracting the molar proportions of P_2O_5 from CaO (McLennan, 1993). If the estimated CaO* was greater than Na_2O, the molar proportion of Na_2O was used, as Ca weathers more readily than Na. Carbonate features were not used in this analysis as they do not reflect the valley's weathering regime.

Principal Component Analysis (PCA) was run for XRF data to reduce dimensionality and interpret elemental relationships and possible transport mechanisms (Jolliffe and Cadima, 2016). Known tephra layers were not included as they do not represent the same depositional regimes as other sediments. PCA was run in R and the code is accessible on GitLab.

4. Results

4.1. Stratigraphy and grain sizes

The KSI sediments, which are measured from the basin floor upwards, include laminated clays, diatomites, silts, fine to coarse sands, carbonates, and tephras (Fig. 2 S1). From 0 to 9 m, the KSI section consists mainly of laminated silty diatomites with laminated silty diatomaceous clays from ~5–6 m (Fig. 2). Carbonate concretions are present at 0.2 m and a black, massive carbonate layer occurs at 2.2 m. Carbonates also occur at 9.2 and 10.25 m and are separated by silty, carbonate-rich clay. The former is black with mm-sized nodules, whereas the latter is gray and irregular with paleoroot fillings. Laminated silts dominate 10.5–12.5 m, above which are beds of fluvial coarse sands. A dated tephra (SUG07-KS-01; Table 1) is present at 14.8 m, with silt above and sandy silt below, both of which contain yellow pumice. Grain size decreases from coarse sands to silts and laminated clays from 13 to 17.9 m. Carbonate content increases from 16 to 17.9 m, where another black, massive carbonate with mudcracks marks a transition to fewer carbonates and more fine-grained sediments. Diatoms are less abundant within the clays from 18 to 21 m. Laminated clayey diatomites and pure diatomites continue to 27.5 m, with bedded carbonate concretions (<20 cm) at 25.3 m. Abundant diatoms disappear above 27.5 m. Above 27.5 m, KSI is coarser grained with numerous tephra horizons interbedded in laminated clayey silts, silts, and silty sands. Alternating pumiceous sand, angular volcanic clasts, bones, burrows, and calcite coatings dominate from 28.5 to 30.5 m. A 20-cm-thick tephra with yellow pumice at 32 m (SUG07-KS-05; T1) is overlain by a 70-cm-thick sand. Carbonate-rich sediments, starting at 33.4 m, include calcareous paleoroots (Fig. 2). The overlying sediments are "baked" carbonate clay with silty components, evidenced by clumped aggregates and discoloration. Sand at ~35.5 m is overlain by clayey and silty deposits with several orange tephra horizons at 41 m (SUG07-KS-2a; Table 1), which have been weathered due to surface exposure and heat-altered by the overlying basalt.

4.2. Chronology and sedimentation rates estimates

A total of 76 grains were analyzed from three samples (S2). Of these, 25 were retained in the calculation of representative mean ages, with the majority of analyses rejected due to anomalously old ages by the gap-finding procedure (42) and an additional four rejected based on plagioclase composition.

The oldest sample (SUG07/KS-1, reworked pumice) shows a simple, quasi-gaussian symmetrical distribution with just one anomalously old analysis out of 17 (Fig. 3A; Table 1) and a MSWD (1.2) close to 1, indicating that analytical errors account for the observed dispersion and that the weighted-mean age of 885 ± 5 ka should provide accurate timing for the source eruption.

The next-oldest sample (SUG07/KS-5, reworked fine pumice and detrital matrix) exhibits 21 analyses registered as anomalously old by the gap-finding technique, leaving nine analyses as a primary mode candidate. The remaining distribution contains two well-defined modes with a high MSWD (8.6), indicating the presence of geological dispersion. Here, the older mode was eliminated on the principle that it may represent xenocrysts not identified by the gap-finding technique, due to the relatively close age proximity to the youngest mode. In fact, the older mode is very similar in age and Ca/K composition to SUG07/KS-1 and may represent incorporation of tephra from that earlier eruption during fluvial transport. After elimination, the remaining five grains give a weighted-mean age of 830 ± 5 ka with a MSWD = 1.5.

The youngest sample (SUG07/KS-2a) was obtained from Plinian fallout ash immediately below the capping mafic lava of the Kamuge-Suguta confluence area. It apparently represents a partially silicic precursor eruptive phase before lava effusion. Most of the 29 grains analyzed were omitted as older contaminants or plagioclase, leaving four K-feldspar grains forming a distinct primary mode with a weighted-mean age of 448 ± 22 ka.

The isochron evaluations of the accepted analyses (Fig. 3B: Table 1) yield ages that are within error of the weighted means and $^{40}Ar/^{36}Ar$ compositions that are indistinguishable from atmosphere (298.56 ± 0.31; Lee et al., 2006). The isochron age errors for samples SUG07/KS-1 and SUG07/KS-4 are equal to or slightly better than the analytical mean errors, however, due to the narrow range of $^{39}Ar/^{40}Ar$ composition and relatively high uncertainty in $^{36}Ar/^{40}Ar$, the isochron regression for sample SUG07/KS-2a yields an error that is about four times that of the weighted mean. For the sake of consistency, the weighted-mean analytical ages and errors are the preferred dating result for all samples.

Given these dates, the ~17.5 m of sediment from 14.8 to 32.25 m represent deposition over ~54 ka, although a potential hiatus exists at 25.3 m. A mean sedimentation rate of ~32.3 cm/kyr (0.3 mm/yr) is estimated, consistent with other estimated diatomite deposition rates across Eastern Africa (c.f. Trauth, 2014) ranging from 10 cm/kyr in the southern Kenya Rift (Owen et al., 2012) to 80–200 cm/kyr at Olorgesailie (Isaac and Isaac, 1977; Potts et al., 1999). With so many potential hiatuses across the record, we were unable to create a reliable age model for this record at this time. Regardless, extrapolation to the base of the section suggests an age of ~931 ka, representing the youngest possible age for the beginning of this section due to several hiatuses. The relatively young age of SUG07/KS-2a suggests at least one large hiatus between 32.5 and 40 m, although multiple breaks in deposition are possible (Fig. 2).

Table 1
Tephra samples with their lithology, location, and data associated with their calculated ages.

Sample	Lab ID	Lithology	Longitude (°E)	Latitude (°N)	n[†]	MSWD[‡]	Ca/K[§]	± Ca/K	Weighted-mean age		Isochron age	
									ka	± 1σ mse[¶]	ka	± 1σ mse[¶]
SUG07/KS-1	25,130	Reworked lapilli	36.293741	1.640124	16/17	1.2	0.004	0.003	**885**	**5**	881	4
SUG07/KS-2a	25,135	Coarse fallout ash	36.293869	1.639776	4/29	1.0	0.02	0.04	**448**	**22**	371	84
SUG07/KS-5	25,148	Reworked lapilli and detrital matrix	36.294238	1.639772	5/30	1.5	0.0	0.2	**830**	**5**	828	5

[†] Number included in weighted-mean over total number of grains.
[‡] Mean square weighted deviation.
[§] Median Ca/K value.
[¶] Modified standard error = standard error multiplied by root MSWD when MSWD>1.

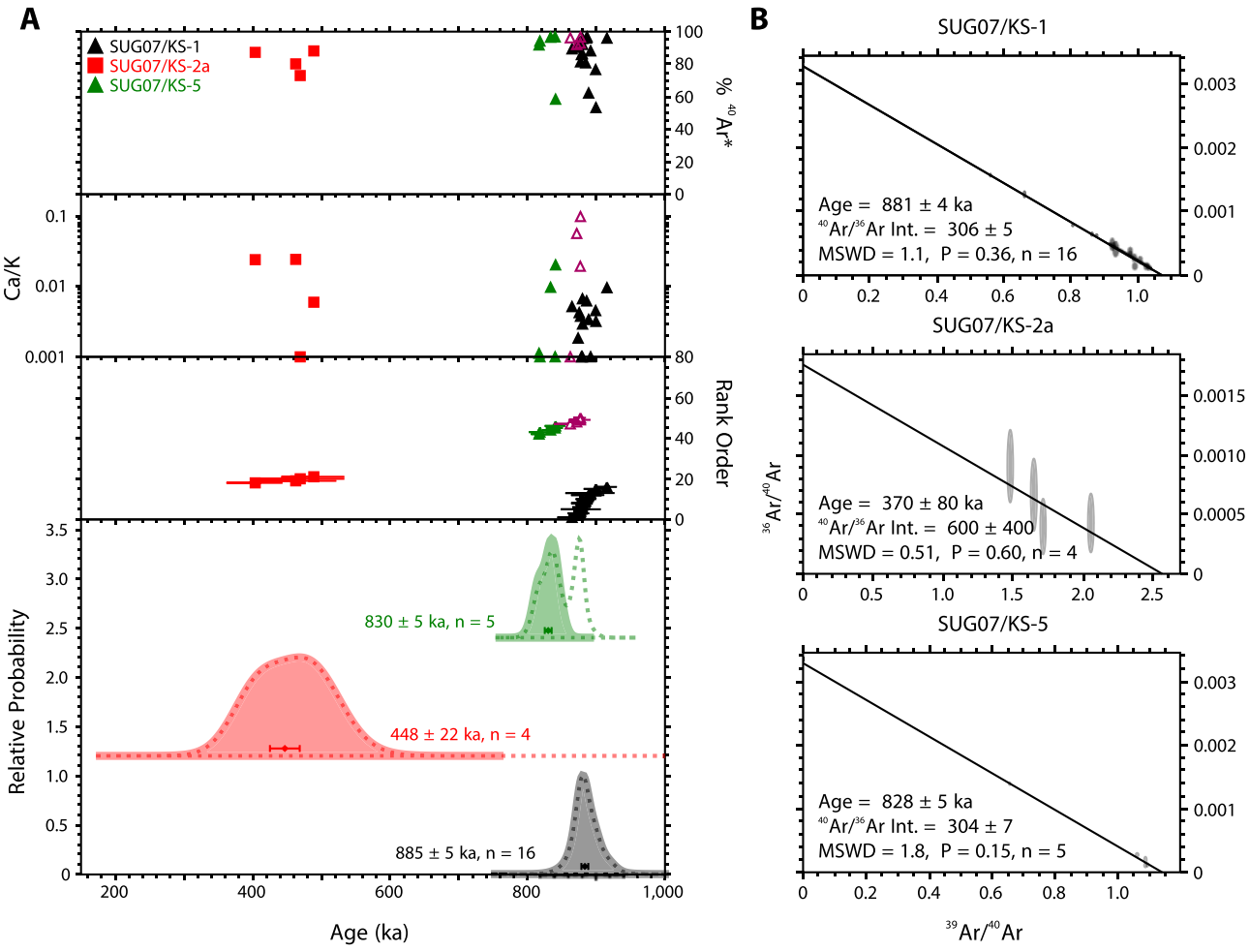

Fig. 3. (A) Age-probability spectra of SCTF analyses. Displayed age range is limited to 150 to 1000 ka; refer to Table 1 for analyses outside this range (all omitted from the accepted age populations). Dashed line represents age-probability density curve of all analyses for a given sample, whereas filled areas represent accepted analyses. Ages shown in text and as error bars are weighted-means with 1- modified standard error. **(B)** 'Inverse' isochron plots (36Ar/40Ar vs. 39Ar/40Ar isotope correlation diagrams) of the accepted SCTF experiments. The isochron age is the x-axis intercept and is shown at 1-. '40Ar/39Ar Int.' refers to 'trapped' non-radiogenic 40Ar/36Ar ratio derived from y-axis intercept of the isochron. 'MSWD' refers to 'mean square of weighted deviates,' a measure of the observed scatter about the t line, compared to the expected scatter. 'P' refers to the probability that the observed scatter can be explained by analytical errors alone. 'n' is the number of analyses.

4.3. Diatom analysis

Diatoms are most abundant in the lower 27.5 m with gaps at 10–12.5, 16–16.5, 18, and 19.5–21 m (Fig. 4; S3). Freshwater, planktonic diatoms are most abundant, particularly *Aulacoseira agassizii* (Ostenfeld) Simonsen, *A. distans* (Ehrenberg) Simonsen, *A. granulata* (Ehrenberg) Simonsen, and *A. granulata* var. *angustissima* (Müller) Simonsen (Figs. 4 and 5; Gasse, 1980; Owen et al., 2014). Notable

exceptions occur at 17 and 17.5 m where >99% of counted taxa are *Stephanocyclus meneghinianus* (Kützing) Kulikovskiy, Genkal & Kociolek (formerly *Cyclotella meneghiniana* Kützing), an indicator of mildly to strongly saline conditions in littoral and planktonic settings (Owen et al., 2014). Shallow water taxa are most abundant from 23.5 to 27 m, where they peak up to 76%. Epiphytic taxa include *Cocconeis placentula* Ehrenberg and *Caloneis bacillum* (Grunow) Cleve, with the latter associated with flowing water. *Hantzschia amphioxys* (Ehrenberg) Grunow and *Luticola mutica* (Kützing) DG Mann are often found in damp soil or swamps. Other freshwater to mildly saline epiphytes and benthic taxa include *Nitzschia amphibia* Grunow, *Epithemia gibberula* (Ehrenberg) Kützing, *E. sorex* Kützing, *Achnanthidium exiguum* (Grunow) Czarnecki, *Sellaphora pupula* (Kützing) Mereschkovsky, and *Staurosira construens* Ehrenberg. Collectively, these taxa indicate fresh, shallow, or swampy conditions perhaps with nearby inflowing streams from 23.5 to 27 m (Owen et al., 2014). Highly saline indicators are absent throughout KSI, indicating that saline phases were not extreme, not preserved, or developed too quickly to be visible at 50-cm intervals.

Of the 82 taxa, 52 are reported within the EDDI (S4). The percentage of taxa missing in the transfer functions ranges from 0 to 36%, averaging to 9.4%. The missing data can be attributed to an irregular *Aulacoseira granulata* morphotype (Plates 17/18/19) also recorded by Gasse (1975), *Epithemia hirundiformis* Müller, and *Nitzschia radicula* Hustedt. *Stephanodiscus neoastraea* Håkansson & Hickel, which was not recognized as a distinct species from *Stephanodiscus astraea* until 1986, is also not in the database, although modern studies show that the ecology is similar to *Stephanodiscus astraea* (Ehrenberg) Grunow (Genkal, 2009). Consequently, these data, which likely include taxa of both *S. neoastraea* and *S. astraea* as one taxon, were used. Absence of data clearly limit the precision of the transfer functions, although comparison with other diatom proxies such as PDI and supplemental XRF data support their inferences. Conductivity is a proxy for salinity within Na_2CO_3-HCO_3 lakes (like many across the EARS), whereas pH provides additional evidence for changes in anionic hydrochemistry (Battarbee, 1986; Gasse et al., 1995). Both measurements, which are closely related in Na_2CO_3-HCO_3 lake systems provide information on the precipitation-evaporation balance of a lake system and are linked with changes in the hydrological budget and climate. Both conductivity and pH remain consistent through the section except at 17 and 17.5 m where they are estimated at ~6030 μS/cm and 8.85, respectively, due to the abundance of *Stephanocyclus meneghinianus* (Fig. 4; S5). The range for other parts of the section are considerably fresher at ~150–870 μS/cm and 7.14–7.91, respectively. PDI ≥ 10 indicates a deep paleolake (Kingston et al., 2007), occurring at 17.8, 18.5, and 23 m.

4.4. XRF analysis and PCA

SiO_2 is the most abundant oxide in the KSI sediments and constitutes 55–65% (median = 59.0%) of the total oxides, except within carbonates (Fig. 6; S6). This reflects opaline silica in diatoms and the strongly silica-oversaturated peralkaline volcanics of the eastern Emuruagiring Plateau and the panterellitic Lower Trachytes of Emuruangogolak (Dunkley et al., 1993). TiO_2 (0.19–2.6%, median = 1.3%), Fe_2O_3 (2.9–13.2%, 9.3%), Al_2O_3 (3.0–18.9%, 15.9%), K_2O (0.4–4.0%, 2.9%), Zr (190–920 ppm, 660 ppm), Zn (40–207 ppm, 164 ppm), and Rb (21–140 ppm, 115 ppm) show similar trends to SiO_2, with respect to the main excursion reflecting igneous sources. In contrast, CaO (0.3–71.3%. 1.7%), MnO (0.08–12.5%, 0.18%), Ba (104–6750 ppm, 373 ppm), Sr (111–1790 ppm, 210 ppm), and LOI (2–37.7%, 9.2%) show similar trends with low values except within carbonates and carbonate-rich sediments, reflecting authigenic and/or biogenic influences. P_2O_5 (0.07–22.5%, 0.28%) is only abundant in carbonates associated with clayey and silty diatomites, reflecting its biogenic nature and potential adsorption within clays. MgO (0.6–5.6%, 1.7%) and Na_2O (1.3–16.6%, 5.0%) do not follow the trends of other oxides, indicating additional controls, such as potential changes in the catchment area or fluvial regime, and their potential for authigenic precipitation during more arid phases.

Carbonates were evident in peaks across all oxide and trace element plots (Fig. 6) and dominated the PCA, with Dimension 1 (Dim1) representing 54.6% of the XRF data trends (S7). Calcareous features, indicated by elevated LOI (Fig. 6), were removed to detrend the data and focus on sediment input. Chromium, Ga, Nb, Ni, V, and Y were not used for analysis as they were detected at low levels, although they tended to reflect deposition from igneous, particularly basaltic, source rocks. With the removal of tephras, carbonates, and less relevant trace elements, Dim1 (38.9%) is significantly controlled by lithogenic elements (Zr, Zn, Al, and Rb in the negative direction), with biogenic/authigenic elements (Sr, Ca, and P) plotting positively (Fig. 7; S7). Dim1 is interpreted as a wetness proxy, where an increase in biogenic/authigenic elements is linked to drier conditions when shallow, nutrient-rich oxygenated waters result in increased biological activity and authigenic precipitation. In contrast, increases in lithogenic elements reflect wetter conditions, when more non-soluble cations are brought into the system as clastics. Dimension 2 (Dim2; 21.4%) is controlled positively by Ti, K, Ba, Fe, and Al and negatively by Mg (with Ca contributing an additional ~5%) (Fig. 7; S7). Positive Dim2 values therefore represent more neutral and wetter settings with negative values indicating saline, alkaline, and drier conditions.

Ti/Ca and K/Al reflect changes in deposition within the alkaline basaltic and trachytic igneous system (Fig. 7; S7). Titanium is an abundant and stable lithogenic element used as a proxy for erosion and transport of silts and fine sands, as it is brought into the system through wind or water transport (Davies et al., 2015). Calcium is a water-soluble element that can be biogenic or lithogenic and allogenic or authigenic, therefore representing sediment input, local precipitation, and/or biological activity. By comparing Ca with Ti, which is not affected by diagenetic overprinting or biological processes (Fitzpatrick and Chittleborough, 2002; Mannella et al., 2019), Ca from igneous sources is removed, leaving biogenic/authigenic Ca depositing over drier phases. Aluminum is an abundant and stable element that is transported through clastic grains, particularly clays. Potassium is water-soluble and abundant in igneous rocks, particularly in trachytes and authigenic clays. When K/Al increases, it reflects a change in clay mineralogy where K fixes during the illitization of smectites in higher pH systems related to drier conditions (Foerster et al., 2018). Both ratios indicate wetter phases from 0 to 9 and 18–27.5 m and drier phases from 9.2 to 17.9 and 28–41 m (Fig. 7).

The mean CIA through the section is 49.1 (Fig. 7). CIA was used to create four zones with constrained hierarchical cluster analysis using Bray-Curtis dissimilarity (CONISS), resulting in boundaries between 8 and 8.5, 18–18.5, and 29–29.5 m. Because these boundaries were created without carbonate features, they were updated to match changes in lithology, resulting in Phase 1 from 0 to 9, Phase 2 from 9.2 to 17.9, Phase 3 from 18 to 27.5, and Phase 4 from 28 to 41 m (Fig. 8; S6). The mean CIA for Phases 1, 2, 3, and 4 are 44.1, 41.4, 58.9, and 48.4, respectively (Fig. 7; S6).

5. Discussion

5.1. Morphological and volcanic history

The morphology of the Suguta catchment during KSI's deposition differed significantly from today, with local volcanoes erupting throughout the Pleistocene and Holocene as rifting widened and deepened the formerly shallow basin (Dunkley et al., 1993). Tephras most likely come from Emuruangogolak or Namarunu despite their ability to travel long distances (>5000 km) within short timeframes (minutes to days) (Lowe, 2011), as most nearby Kenya Rift volcanoes are younger than KSI (Dunkley et al., 1993). The trachytic shield of Emuruangogolak began forming 900 ± 100 ka and continued to develop until 500 ± 100 ka (Weaver, 1977; Dunkley et al., 1993), with dated Emuruangogolak eruptions at 864 ± 7 ka (Dunkley et al., 1993). At Namarunu, two

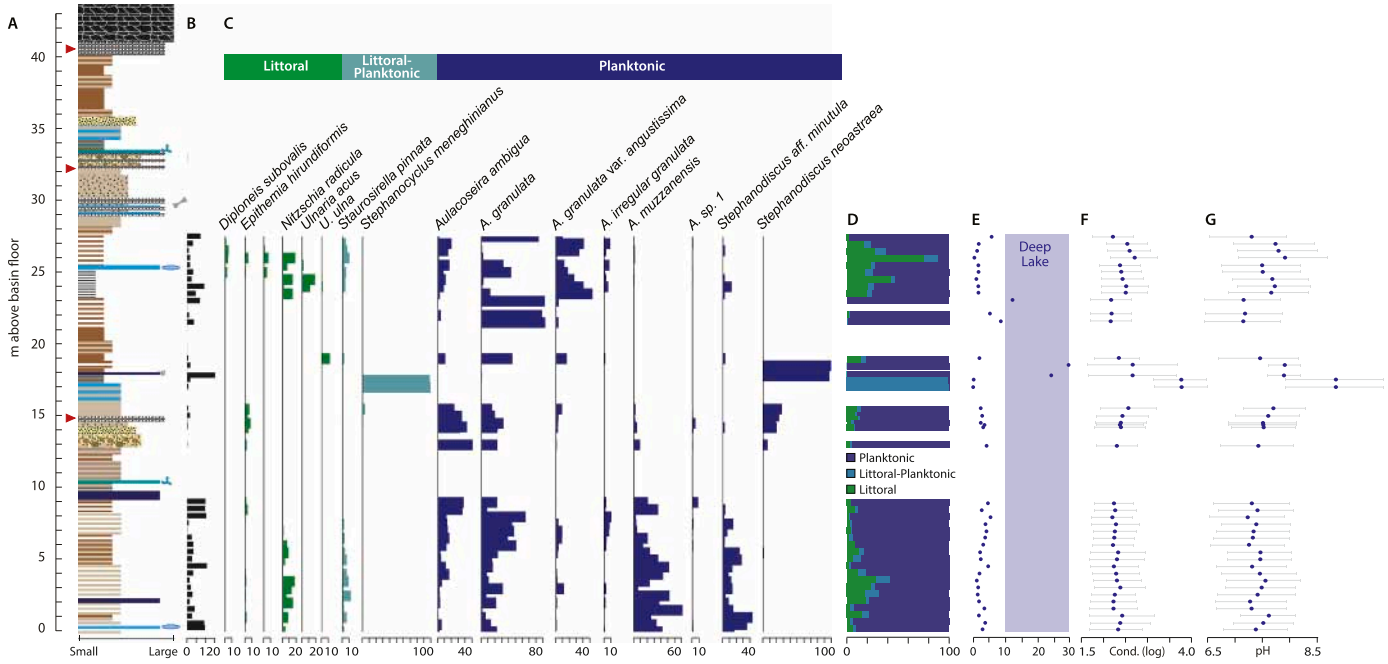

Fig. 4. **(A)** KSI lithological column. **(B)** Diatom concentration. **(C)** Diatom species percentages for taxa that make up at least 5% of one sample. Diatom species are organized by littoral, littoral planktonic, and planktonic species. **(D)** Diatom habitat preferences. **(E)** Planktonic Diatom Index (PDI). **(F)** Conductivity based on Gasse et al. (1995) transfer function with the tolerance range. **(G)** pH based on Gasse et al. (1995) transfer function with the tolerance range.

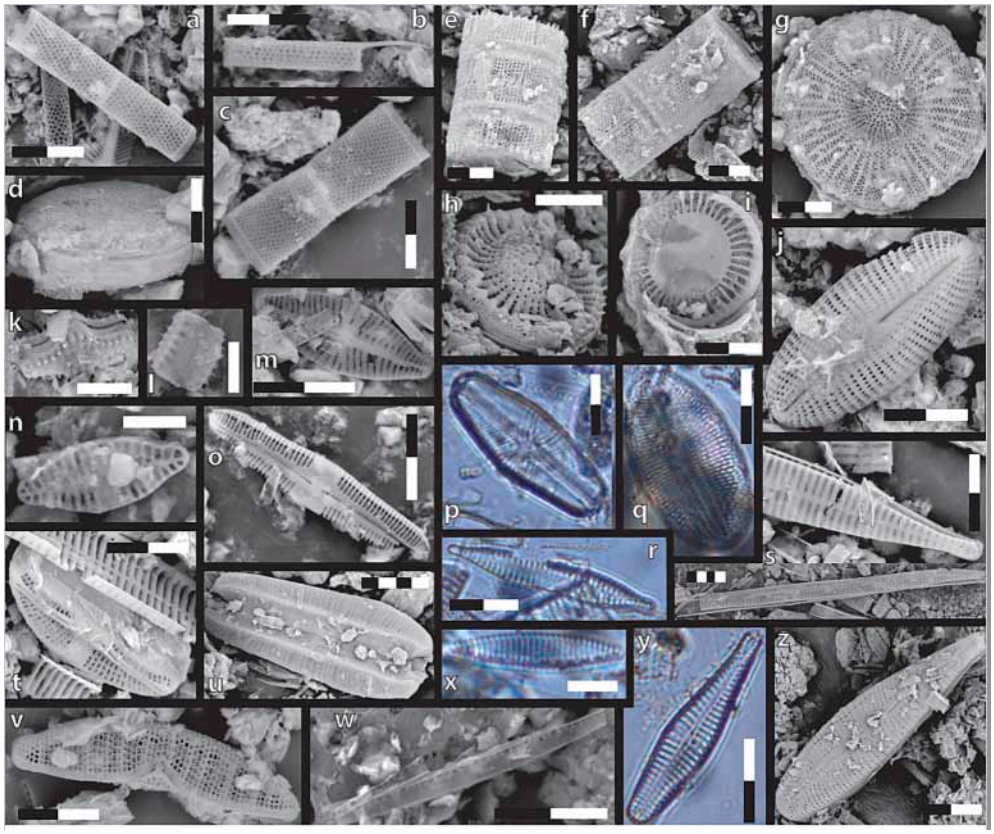

Fig. 5. SEM and light microscope photographs of some of the most common diatoms. Each black or white part of the scale bar is 5 μm. Identifications: **a** *Aulacoseira granulata* (Ehrenberg) Simonsen; **b** *Aulacoseira granulata* var. *angustissima* (Müller) Simonsen; **c** *Aulacoseira granulata* var. irregular; **d** *Thalassiosira rudolfi* (Bachmann) Hasle; **e** *Aulacoseira agassizi* (Ostenfeld) Simonsen; **f** *Aulacoseira muzzanensis* (Meister) Krammer; **g** *Stephanodiscus neoastraea* Håkansson & Hickel; **h** *Stephanodiscus* cf. *minutulus* (Kützing) Cleve & Möller; **i** *Stephanocyclus meneghinianus* (Kützing) Kulikovskiy, Genkal & Kociolek (formerly *Cyclotella meneghiniana* Kützing); **j** *Diploneis subovalis* Cleve; **k** *Staurosira construens* Ehrenberg; **l** *Staurosirella pinnata* (Ehrenberg) Williams & Round; **m** *Geissleria decussis* (Hustedt) Lange-Bertalot; **n** *Planothidium rostratum* (Oestrup) Round & Bukhityarova; **o** *Caloneis bacillum* (Grunow) Cleve; **p** *Sellaphora pupula* (Kützing) Mereschkovsky; **q** *Cocconeis placentula* var. *euglypta* (Ehrenberg) Grunow; **r** *Fragilaria capucina* var. *vaucheraie* (Kützing) Lange-Bertalot; **s** *Ulnaria acus* (Kützing) Aboal; **t** *Amphora copulata* (Kützing) Schoeman & Archibald; **u** *Epithemia hirundiformis* Mueller; **v** *Epithemia adnata* (Kützing) Brébisson; **w** *Nitzschia* cf. *radicula* Hustedt; **x** *Nitzschia* cf. *paleacea* (Grunow) Grunow; **y** *Gomphonema* aff. *Intricatum* Kützing; and **z** *Gomphonema* cf. *olivacoides* Foged.

eruptions took place during KSI's deposition at 871 ± 5 and 840 ± 5 ka (Dunkley et al., 1993). Older local basalts (4–2.33 Ma) from Namarunu (Dunkley et al., 1993) may have contributed to KSI's sedimentary basaltic influx.

5.2. Lithological deposition

Dunkley et al. (1993) observed that the capping basalt, 25 m southwest of KSI, overlies poorly stratified and cross-stratified sands cut

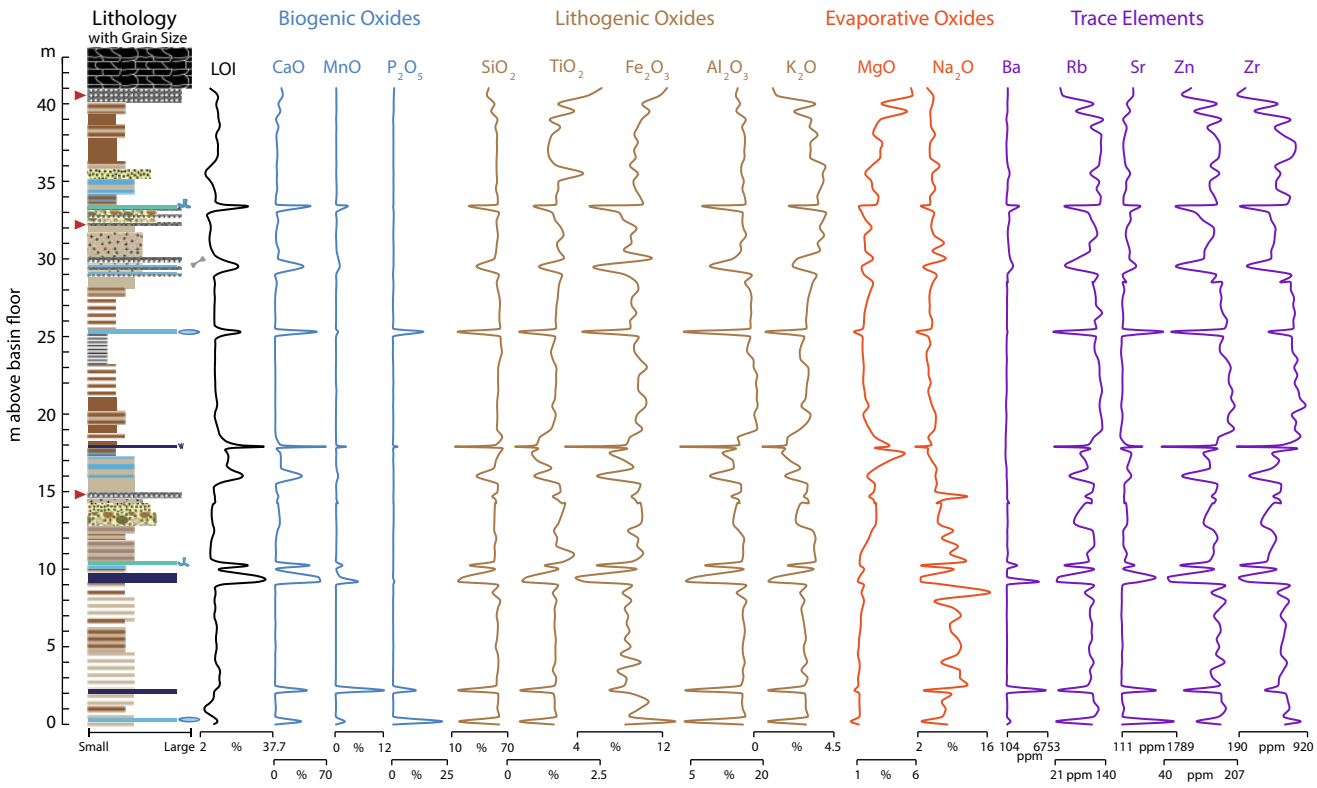

Fig. 6. KSI lithographic column with XRF results, including Loss on Ignition (LOI), normalized oxides organized by potential origins, and trace elements Ba, Rb, Sr, Zn, and Zr that were included in the Principal Component Analysis (PCA). Plots were smoothed with exponential smoothing. Major spikes indicate carbonate rich layers across nearly all plots.

by large channels. These sands indicate nearby fluvial conditions, which may have eroded several hiatuses at KSI, thus explaining the large age gap in the upper sequence. Older sands at KSI support Truckle's (1976 & 1977) suggestion that Paleolake Suguta, despite being laterally extensive, was at least periodically shallow. Rapid lateral facies variations might reflect delta/fan switching (sedimentary control) and/or lake level variations (a climatic control). The latter scenario would imply rapid changes from deep water (laminated diatomites) to shallower lakes with alluvial fans and deltas.

Clays likely also indicate phases of fluvial deposition, with mixed lithologies and graded bedding likely representing direct riverine deposition, and interbedded clays and silt to fine sands representing flood plains. Fluvial clays may have also been transported into deeper lake waters as hypopycnal or hyperpycnal flows where they would have become interbedded with diatomites on a seasonal or longer-term basis. Today, cm-scale clastic laminae related to seasonal Omo River flooding into Lake Turkana are a modern example of laminated clays being preserved in fully oxygenated water tens of meters deep (Cohen, 1984). Other clays may represent authigenic clays which are well-documented across Eastern Africa such as at Chew Bahir (Foerster et al., 2018), although further studies of the mineral composition are necessary to distinguish between authigenic and allogenic clays.

5.3. Biological deposition

O'Sullivan (1983) recognized four types of laminations in lakes: ferrogenic, calcareous, biogenic, and clastic. He noted that a flat basin morphometry (reduced slumping and lateral creep) and periodicity in sediment supply are important. In addition, deep waters prevent wind-induced lake floor reworking and favor anoxic bottom conditions and organic preservation with suppression of infauna, preserving laminae. This is the case at Lake Malawi where mm-scale *Aulacoseira-Stephanodiscus-Nitzschia* laminae are common (Owen and Crossley, 1992; Pilskaln and Johnson, 1991). In some circumstances, however, shallow, highly saline lakes can preserve lamination due to infauna inhibition. Strong chemical stratification can also prevent wind-induced disturbance in waters 1–2 m deep, as is the case at Nasikie Engida in the South Kenya Rift (Renaut et al., 2021). Therefore, while deep lakes can preserve laminated diatomites, evidence across Eastern Africa indicates that shallower lakes can preserve laminae as well.

Three diatomite facies are distinguished in KSI: **a)** finely laminated diatomites (mm-thick); **b)** laminated clayey diatomites (<1 cm); and **c)** laminated silty diatomites (1–2 cm) (Fig. 2). Facies 1 and 2 often have a higher concentration of diatoms than Facies 3. **a)** The finely laminated diatom layers at 23.5–25 m indicate deep water with high percentages of *Aulacoseira granulata,* that is favored by deep, silica-rich waters and high wind turbulence, and long, thin benthic taxa, that can be transported into deeper waters, including *Ulnaria acus* (Kützing) Aboal and *Nitzschia radicula* (Gasse, 1986). **b)** The laminated clayey diatomites host variable communities, including shallow- and deep-water taxa, suggesting mixed flora from different settings. The inclusion of *Aulacoseira* (*A. ambigua* (Grunow) Simonsen, *A. granulata* var. *angustissima*) that occur in shallow to moderate water, also indicates deposition from variable lake depths. **c)** Laminated silty diatomites only occur in the lower sequence. Parts of the laminated sequence where benthic taxa are common may reflect shallowing events with subsequent floral mixing during deposition or sampling. Littoral and/or fluvial taxa can also be introduced from nearby rivers (Barker et al., 1991).

Five carbonate types are present at KSI: **a)** yellow, disk-like layered concretions <20 cm in diameter; **b)** flat, irregular, gray, and coarse-grained carbonates; **c)** dark (almost black) hard layers with mm-scale nodules; **d)** carbonate-rich clays and silts; and **e)** soil carbonates (Fig. 2). Such a variety in fluvio-lacustrine deposits is common in Eastern Africa, with the Plio-Pleistocene fluvio-lacustrine sediments and carbonate layers of Olduvai basin providing prime examples (Hay, 1976; Cerling and Hay, 1986; Bennett et al., 2012; Liutkus et al., 2005; Ashley

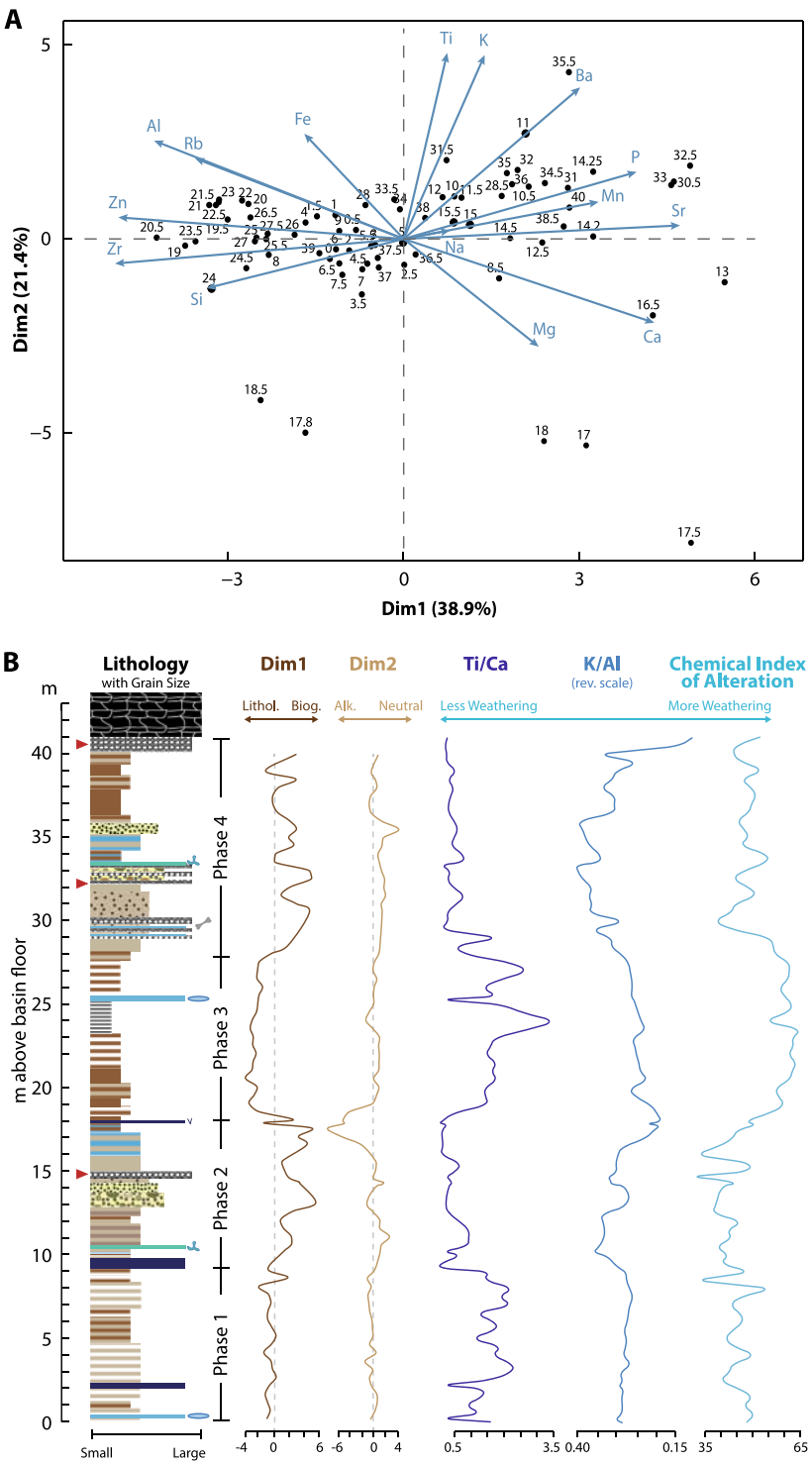

Fig. 7. **(A)** Biplot of the Principal Component Analysis (PCA) of major oxides and trace elements Ba, Cr, Rb, Sr, Zn, and Zr. Dimension 1 (Dim1) represents 38.9% of variability which is interpreted as biogenic/authigenic vs. lithogenic elements. Dimension 2 explains 21.4% and is interpreted as alkaline vs. neutral waters (S7). Elements that are considered having significant control over the dimensions represent higher than average impact on the dimension. **(B)** Lithographic column with Dim1 and Dim2 loadings of the PCA, Ti/Ca, K/Al in the inverse, and the Chemical Index of Alteration (CIA). Plots were smoothed with exponential smoothing.

et al., 2014; Stanistreet et al., 2020). **a)** The disk-like concretions occur twice in the record, close to lithological changes towards coarser sediments. Stanistreet et al. (2020) and Bennett et al. (2012) describe similar carbonates as accretional nodules just below erosional surfaces, reflecting secondary growth. Erosional features were not observed at KSI but are not excluded given the lithological changes. If hiatuses exist, then they were short-lived, as there are no well-developed soils (Stanistreet et al., 2020). **b)** Flat, gray, coarse-grained carbonates occur in silty clays and sands and are interpreted as algal mats in shallow, stagnant waters, representing primary carbonate. **c)** Dark, thin (<5 cm) carbonate layers in clays, silts, and clayey carbonates indicate shallow, alkaline waters, resulting in the precipitation of primary carbonates. **d)** Calcareous clays are secondary, likely forming when Paleolake Suguta dried, given that similar carbonate (and gypsum) crusts are observed today (Dunkley et al., 1993). **e)** Secondary soil carbonates form after desiccation and indicate hiatuses.

5.4. *Paleoenvironmental reconstructions*

5.4.1. *Phase 1 (0–9 m, >885 ka): freshwater lake*

The mostly laminated silts and diatomites from 0 to 9 m indicate deposition in a freshwater lake with variable water depth. High Ti/Ca

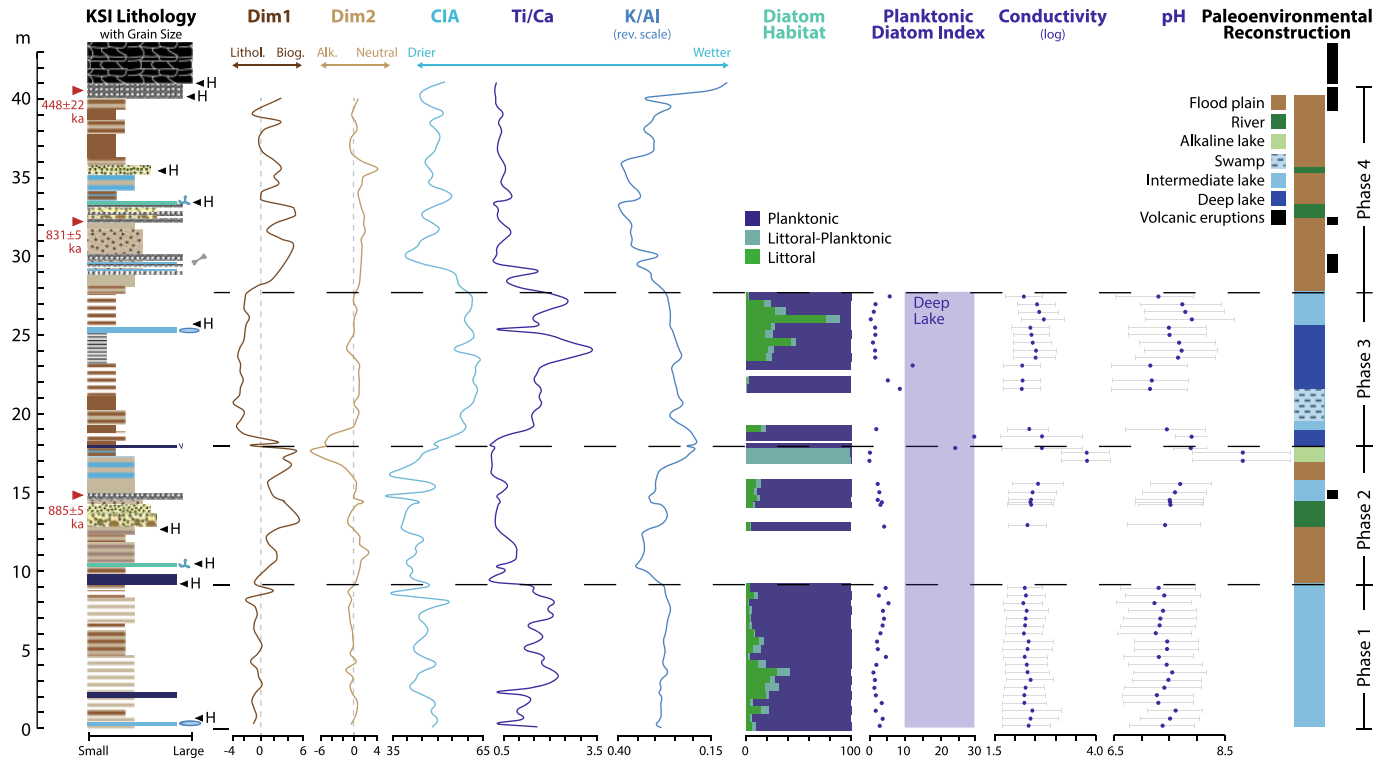

Fig. 8. Lithogenic column divided into the four phases with important data and interpretations from the multiple proxies in this study, including stratigraphic analysis, PCA (Dim1 and Dim2), CIA (Nesbitt and Young, 1982), XRF ratios (Ti/Ca and K/Al), diatom habitat, PDI (Kingston et al., 2007), and transfer function parameters including conductivity in log and pH (Gasse et al., 1995). Data were used to create a paleoenvironmental reconstruction that includes phases of volcanics within KSI.

and low K/Al ratios reflect silty clastic inputs during shallow phases, with a mean CIA of 44.1, suggesting low to moderate weathering in the catchment (Fig. 8). Carbonate concretions at 0.2 m indicate a hiatus. Abundant planktonic taxa, including *Aulacoseira ambigua, A. granulata, A. muzzanensis,* and *Stephanodiscus* cf. *minutulus* (Kützing) Cleve & Möller (Fig. 2), imply both shallow and deeper lakes during Phase 1. From 2 to 4 m, littoral taxa (*Epithemia*, *Gomphonema, Nitzschia* spp.*)* constitute 11.3–29.0% of the assemblage, indicating a shallower stage. A black, primary carbonate at 2.2 m supports this conclusion. Increased *A. ambigua* percentages across the rest of the phase suggests that waters were of intermediate depth, with PDI < 10 across the section. The transfer functions indicate an average conductivity of only ~310 µS/cm and pH of 7.36 (Fig. 8), implying an open lake and wet climate. Phase 1 ends with a black, precipitated carbonate at 9.2 m, increased LOI, and a disappearance of diatoms, representing potential desiccation.

5.4.2. *Phase 2 (9.2–17.9 m, ~885 ka): fluvial and flood plains with temporary standing water*

Sediments at 9.2–17.9 m are more variable than the rest of the sequence, with silty clay to coarse sands indicating river settings and flood plains with episodic lakes (Fig. 8). An increase in biogenic/authigenic input, reduced Ti/Ca and enhanced K/Al ratios, and decreased CIA (41.2), also suggest a drier climate with less weathering compared to Phase 1. SUG07/KS-1 at 14.7 m is dated to 885 ± 5 ka (Table 1), with potential hiatuses at 10.2 and 13 m. Non-diatomaceous laminated silts and clays (9–13 m) suggest a flood plain begins this phase. Carbonate crusts with high LOI and rhizoliths indicate land surfaces, possibly with highly alkaline ephemeral waters with algal mats. The lack of diatoms could reflect high pH waters that prevented diatom growth and/or competitive exclusion or post-mortem dissolution (Barker et al., 1994; Ryves et al., 2013). Sands (13–14.2 m) suggest fluvial conditions followed, with a possible erosion surface at 13 m. Diatoms (*Aulacoseira* spp., *Epithemia hirundiformis*) at 14.2–15.5 m indicate a freshwater lake. Diatoms are absent at 16–17 m reflecting either short-term desiccation or highly alkaline conditions, supported by the presence of carbonates and calcareous silty clays. Diatoms at 17–17.5 m are dominated by *Stephanocyclus meneghinianus* with low diversity, suggesting a highly alkaline lake (average conductivity and pH of ~5970 µS/cm and 8.85, respectively; Figs. 4 and 8). Black carbonate at 17.9 m suggests alkaline conditions and potential desiccation.

5.4.3. *Transition from phase 2 to phase 3*

The Phase 2 to 3 diatom transition indicates major changes within a short stratigraphic interval that deviate from KSI's generally freshwater *Aulacoseira*-dominated communities. At 17 and 17.5 m, assemblages are >98% *Stephanocyclus meneghinianus*, a mostly shallow and saline water indicator (Fig. 4; Gasse, 1986; Owen et al., 2014). In contrast, at 17.8 m, *Stephanodiscus neoastraea* (>97%) indicates a major shift to fresher, deeper water, also evidenced by the transfer functions and PDI. Diatoms disappear at 17.9 (a black carbonate) and 18 m (carbonate-rich layered clays and silts), ultimately returning at 18.5 m with >99% *S. neoastraea*. The most significant change across Dim2 also occurs here with negative values at ~16–19 m, reflecting increased carbonate precipitation (Fig. 8), which is also evident in increased MgO from 10 to 17 m (Fig. 6). With a sedimentation rate of 32.3 cm/kyr, it is unlikely that this major change is the result of a long-term hiatus between these points. In addition, there is no sedimentological evidence for a substantial hiatus, with mudcracks within the black carbonate representing temporarily dry conditions. Paleolake Suguta therefore changed from a shallow, saline, and even desiccated lake into a deeper, freshwater lake over hundreds of years, mirroring rapid responses to changing climate during the AHP (Bergner et al., 2009; Olaka et al., 2010; Trauth et al., 2010; Garcin et al., 2012; Junginger and Trauth, 2013; Junginger et al., 2014). Limiting nutrients might also partly explain the unusual increase in *S. neoastraea* and could reflect changes in source water, depth, mixing, or seasonality given its abundance in low Si:P environments (Kilham

et al., 1986). None of these hypotheses are mutually exclusive and can all be partially linked to depth variations. It is conceivable that this is not the only part of the sequence that changed rapidly, but at 50-cm resolution, such events may have been missed.

5.4.4. *Phase 3 (18–27.5 m, >831 ka, <885 ka): highly fluctuating lacustrine conditions*

Laminated clays, silts, and diatomites dominate 18–27.5 m, indicating a variable lacustrine phase (Fig. 8). Increased clastics and Ti/Ca, decreased K/Al, and abundant *Aulacoseira* similarly reflect a paleolake. The CIA average of 58.9 indicates more heavily weathered source rocks compared to the rest of the outcrop. Major increases and decreases in water levels over millennia are indicated by rapid transitions from shallow, alkaline diatoms (17.5 m) to freshwater taxa (17.8 m) and the development of mudcracks (17.9 m) as discussed in 5.4.3. Diatoms are absent at 18 m, but give way to deep, freshwater taxa at 18.5 m. At 19 m, a low concentration of diatoms indicates a shift to shallower conditions with the return of littoral and littoral-planktonic assemblages, supported by a slight increase in K/Al and less stratified clays and clayey silts. *Ulnaria ulna* (Kützing) Compère makes up 12.4% of the assemblage at 19 m and could signal swampy conditions, although this taxon can be reworked into the plankton (Gasse, 1986; Owen and Renaut, 2000). Diatoms are absent at 19.5–21 m, which has high CIA and Ti/Ca. The laminated silts and clays are interpreted as a shallow, alkaline swamp in which the diatom frustules may have dissolved. At 21.5–23 m, the assemblage is dominated by *A. granulata*, indicating deeper water

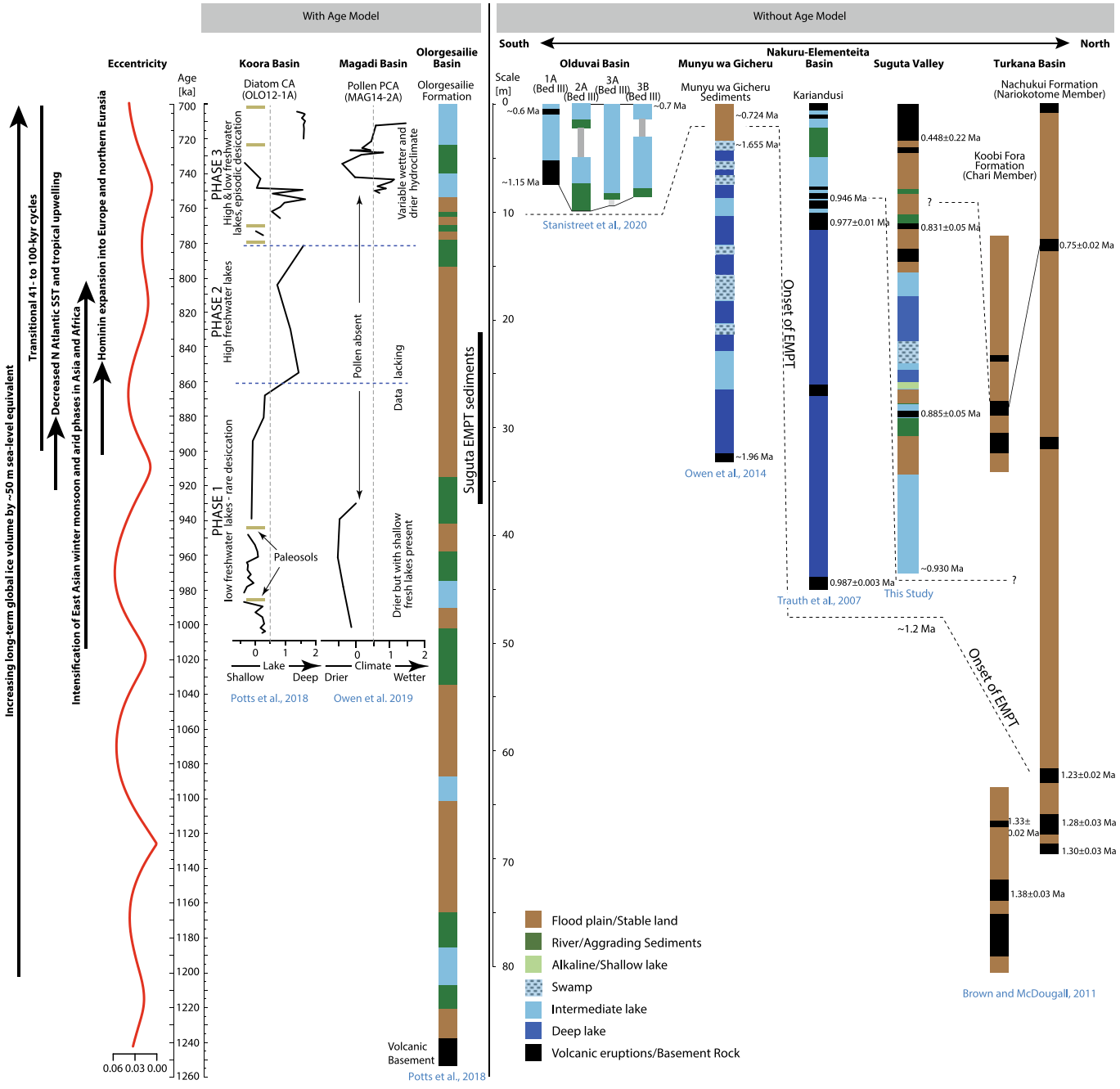

Fig. 9. Comparison of records across the Eastern Branch of the EARS that are included in the text separated by those with an age model and those without, highlighting the lack of temporal resolution throughout the region. Sources within include (Brown and McDougall, 2011; Owen et al., 2014; Potts et al., 2018; Stanistreet et al., 2020; Trauth et al., 2007; Owen et al., 2019). In addition, a comparison with eccentricity and known changes of the EMPT are included.

(Fig. 4). Diatoms are scarce at 22.5 m but *A. granulata* are dominant (55/75 counted valves), which is interpreted as due to diagenesis rather than desiccation based on the lack of other clear evidence for desiccation. Finely laminated diatomaceous layers at 23.5–25 m indicate deep water, although increased *A. granulata* var. *angustissima* may reflect shallower influences. These deposits are also associated with long, thin littoral taxa (*Ulnaria*, *Nitzschia*) (Gasse, 1986). Owen and Renaut (2000) reported mixed *Aulacoseira-Synedra* (*Ulnaria*) from similar mm-scale laminated Miocene diatomites in the Tugen Hills as deep-water floras, noting that the diatoms might represent a seasonal succession controlled by Si:P ratios (Kilham et al., 1986). The presence of carbonate concretions at 25.3 m indicates a potential hiatus, although the diatom assemblages between 25 and 27 m have similarly high percentages of *A. granulata* with increasing *A. granulata* var. *angustissima*. At 27.5 m, *A. granulata* dominates again before diatoms disappear permanently.

5.4.5. Phase 4 (28–41 m, ~831, >448 ka): fluvial and flood plain deposition

Non-diatomaceous laminated silts, carbonates, sands, sandy calcareous tephra, and tephra layers from 28 to 41 m indicate rivers and flood plains during this phase (Fig. 8). The shift to biogenic/authigenic deposition, decrease in Ti/Ca, and gradual increase in K/Al support this suggestion. Diatoms are scarce throughout this phase, with the area perhaps flooding occasionally, such as at 33 m where 26/35 diatoms are *Aulacoseira*. This is supported by a nearly 1-m-thick marker horizon of pumice and riverine sands in a carbonate matrix with bones (fish, turtle, crocodile, antelope). Increased volcanic activity is indicated by elevated Cr, Ni, Mg, V, Fe, and Ti which are at their highest concentrations in the KSI record (Fig. 6; S6). The large timeframe between 831 ± 5 ka (32.25 m) and 448 ± 22 ka (41.5 m) indicates either a decrease in sedimentation rate and/or one or more hiatuses, potentially at 33.4, 35.5, 40.5, and 41 m.

5.5. Regional comparison and relation to the EMPT

Earlier reviews of Eastern African Pleistocene environments around the EMPT note that freshwater lakes existed between 1100 and 900 ka during a humid period extending between southern Arabia (Nicholson et al., 2020), the Afar Basin in northern Ethiopia (Gasse, 1990; Trauth et al., 2005, 2007), and the Olorgesailie Basin in southern Kenya (Fig. 9; Owen and Potts, 2009; Trauth et al., 2009; Trauth et al., 2015). The EMPT represents the change from 41- to 100-kyr glacial cycles and increasing long-term global ice volume by ~50 m sea-level-equivalent from 1200 to 700 ka (Pisias and Moore, 1981; Clark et al., 2006; Maslin and Brierley, 2015). Across the EMPT, sea surface temperatures in the North Atlantic and tropical ocean upwelling regions decreased, particularly from 920 to 880 ka, leading to an intensification of the East Asian winter monsoon and arid phases in Asia and Africa (Clark et al., 2006; Sun et al., 2006; Head et al., 2008; Lee et al., 2020). In addition, there is evidence for an increase in North Atlantic Deep-Water formation (Martin-Garcia et al., 2018), a reduction of North Atlantic thermohaline circulation (Clark et al., 2006; Head et al., 2008), and an increase in Walker circulation (McClymont and Rosell-Melé, 2005), particularly around 900 ka. These global changes, that expanded grassland biomes during intensification of glacial cycles and colder climates, resulted in mass migration of mammals globally (Azzaroli et al., 1988; Head and Gibbard, 2005; Martínez-Navarro and Rabinovich, 2011; van Kolfschoten and Markova, 2005; Vrba, 1996), including members of our genus Homo (deMenocal, 2004; Head and Gibbard, 2005). Global changes during the EMPT are highlighted in Fig. 9.

Regional comparison of paleoenvironmental change along the Gregory Rift between ~931–831 ka is difficult given the lack of well-constrained age models and paleolake records (Fig. 9). Recent core records from the Koora Basin shed light on the EMPT with three hydroclimatic phases evident from diatoms (Muiruri et al., 2021a). Phase 1 (~1000–860 ka) was characterized by shallow fresh lakes with two desiccation episodes. The paleolakes then deepened during Phase 2 (~860–780 ka) and remained high. Phase 3 (780–700 ka) shows greater variability with shallow and deep lakes that periodically dried out. At Lake Magadi, located within 20 km from the Koora Basin, pollen are not preserved between 940 and 750 ka, but earlier floras suggest stable drier climates with more varied conditions after ~750 ka (Muiruri et al., 2021b). Olorgesailie, located just north of Koora and Magadi, was dominated by terrestrial sediments through much of the EMPT (with a lake only developing at ~980 ka), but with two wetter intervals during Phase 3 that match the later wetter conditions at Koora and Magadi (Potts et al., 2018).

The KSI deposits represent two lacustrine intervals with variable lake levels that are suggestive of broadly wetter conditions. The first developed by >931 ka with the second after 885 ka and ceasing before 831 ka, spanning the major Phase 1 to 2 transition at Koora. The first lake expansion does not match well with Phase 1 low levels at Koora. However, the second may reflect the major Koora deepening at 860 ka, which peaked at about the same time at MIS21g (Muiruri et al., 2021a). Regardless, such variability highlights the intense changes that occurred globally around 900 ka (Fig. 9). Other parts of the EMPT are less comparable, possibly because of the impact of local tectonics, volcanism, autocyclic sedimention, variability between chronological models (Muiruri et al., 2021a), and heightened environmental changes associated with the EMPT. Indeed, Potts et al. (2020) noted difficulties in their attempts to correlate between Koora lake levels and global climate, especially before 500 ka.

Detailed comparisons are even more difficult elsewhere. At Olduvai Gorge, Bed III claystones and sandstones (1.15–0.70 Ma) indicate rivers and shallow waters during the early EMPT (Fig. 9; Stanistreet et al., 2020). At Munyu wa Gicheru, multiple lacustrine phases (1.96–1.65 Ma) led into terrestrial conditions at 1.65–0.724 Ma (Owen et al., 2014). Further north of Munya wa Gicheru, at Kariandusi in the Elmenteita-Nakuru Basin, a 31-m-thick diatomite (~0.987 Ma–post-0.946 Ma) documents a deep, freshwater lake. This large palaeolake ceased with the development of cross-bedded sands and relatively thin diatomites (Trauth et al., 2007). Floodplains dominated the Turkana Basin during the EMPT, with erosion removing ~1–0.8 Ma records at Koobi Fora (Brown and McDougall, 2011). With no hydrological separation evident during KSI's deposition (McDougall et al., 2012), the KSI section could represent a southern extension of a Suguta/Turkana megalake with the lack of evidence for Paleolake Turkana related to burial below the modern lake and erosion of marginal areas.

6. Conclusions

Reviews of EMPT records in Eastern Africa show, like global climate records, that lake dynamics across the EARS varied through space and time. KSI provides insights into changes of Paleolake Suguta between >931–831 ka. Dates of 885 ± 5 and 831 ± 5 ka in the middle of the outcrop, allowed reconstruction of lake dynamics across the later EMPT. The KSI record indicates two wetter and two drier intervals. Shallow, intermediate, and deep freshwater lakes developed by at least ~931 ka with drier conditions setting in before 885 ka. The second lacustrine interval was characterized by variable freshwater, shallow to deep, paleolakes, and a closed-basin lake with higher salinities. These paleolakes appear to have changed from one state to another over a scale of hundreds of years leading to the development of a drier flood plain some time before 831 ka.

The Suguta record documents how variable EMPT humid phases were at a fine scale, reflecting the profound global climatic changes during this time. Comparisons with core records from the southern Kenya Rift show generally poor correlations for these detailed phases, likely reflecting the impacts of tectonism, volcanism, and autocyclic sedimentation on local paleoenvironments. However, the onset of deeper lakes at Koora appear to have developed at about the same time as the second lacustrine interval at Suguta and led to major lake

expansions in both basins, peaking during oxygen isotope stage 21g, and perhaps reflecting a major inflection in the global climate record.

Supplementary data to this article can be found online at https://doi.org/10.1016/j.palaeo.2023.111758.

Declaration of Competing Interest

The authors declare that they have no known competing financial interests or personal relationships that could have appeared to influence the work reported in this paper.

Data availability

Data and code for this project are available on GitLab: https://gitlab.com/robakiewicz-micropaleontology-and-paleoclimatology/ksi-code

Acknowledgements

Thank you to the two anonymous reviewers who provided constructive feedback on this manuscript. Thank you to Ines Bludau, Lisa Park Boush, Ran Feng, and Christian Tryon for their help in early edits and discussions of these data. Thank you to Tatiana Miranda for help on the SEM. Thank you to Dan Olago for his help in the acquisition of local geologic maps of Kenya used to create Fig. 1C. Thanks to the Deutsche Forschungsgemeinschaft for their funding of the Suguta Valley Project by M.T. and M. Strecker (DFG TR 419/6, June 1, 2007 – December 31, 2014). E.R. acknowledges 2019 Charles A. & June R.P. Ross Research Funding through the Geological Society of America used for this project. This research is also part of "Wet Feet or Walking on Sunshine" awarded to A.J., funded by the Ministry of Culture and Science (MWK) of Baden Württemberg, the University of Tübingen, and Senckenberg Centre for Human Evolution and Paleoenvironment, Germany. Funding was also awarded to R.B.O. by the Research Grant Council Hong Kong for the project "Temporal variations in the controls of lacustrine sedimentation during continental rift evolution: evidence from the northern Kenya Rift Valley." S.K. also acknowledges funding from the Deutsche Forschungsgemeinschaft (DFG KU 3512/2-1, project-No. 408311491). C.R. acknowledges funding from the Federal Ministry of Education and Research, the Baden-Württemberg Ministry of Science, and University of Tübingen as part of the Excellence Strategy of the German Federal and State Governments (PRO-ROSCA-2021-11).

References

Ackermann, E., Heinrichs, T., 2001. Geologie-Ostafrika, Vol. 1, 1000000 Deutsche Forschungsgemeinschaf.

Ashley, G.M., Beverly, E.J., Sikes, N.E., Driese, S.G., 2014. Paleosol diversity in the Olduvai Basin, Tanzania: effects of geomorphology, parent material, depositional environment, and groundwater on soil development. Quat. Int. 322–323, 66–77. https://doi.org/10.1016/j.quaint.2013.12.047.

Azzaroli, A., De Giuli, C., Ficcarelli, G., Torre, D., 1988. Late Pliocene to Early Mid-Pleistocene Mammals in Eurasia: Faunal Succession and Dispersal Events. Palaeogeogr. Palaeoclimatol. Palaeoecol. 66 (1), 77–100. https://doi.org/10.1016/0031-0182(88)90082-X.

Baker, B.H., 1963. Geological Map of the Baragoi Area, , 53rd ed.Vol. 1. Ministry of Commerce & Industry Mines and Geological Department Kenya. 125,000.

Baker, B.H., Wohlenberg, J., 1971. Structure and evolution of the Kenya Rift Valley. Nature (London)Nature 229 (5286), 538–542. https://doi.org/10.1038/229538a0.

Barker, P., Gasse, F., Roberts, N., Taieb, M., 1991. Taphonomy and Diagenesis in Diatom Assemblages; A Late Pleistocene Palaeoecological Study from Lake Magadi, Kenya, Vol. 214.

Barker, P., Fontes, J.-C., Gasse, F., 1994. Experimental dissolution of diatom silica in concentrated salt solutions and implications for paleoenvironmental reconstruction. Limnol. Oceanogr. 39 (1), 99–110. https://doi.org/10.4319/lo.1994.39.1.0099.

Battarbee, R.W., 1986. Diatom analysis. In: Berglund, B.E. (Ed.), Handbook of Holocene Palaeoecology & Palaeohydrology, pp. 527–570.

Battarbee, R.W., Juggins, S., Gasse, F., Anderson, N.J., Bennion, H., Cameron, N.G., Ryves, D.B., Pailles, C., Chalie, F., Telford, R., 2001. European Diatom Database (EDDI). An information system for palaeoenvironmental reconstruction. ECRC Research Report (81), 1–94.

Bennett, C.E., Marshall, J.D., Stanistreet, I.G., 2012. Carbonate horizons, paleosols, and lake flooding cycles: beds I and II of Olduvai Gorge, Tanzania. J. Hum. Evol. 63 (2), 328–341.

Bergner, A.G.N., Strecker, M.R., Trauth, M.H., Deino, A., Gasse, F., Blisniuk, P., Dühnforth, M., 2009. Tectonic and climatic control on evolution of rift lakes in the Central Kenya Rift, East Africa. Quat. Sci. Rev. 28 (25), 2804–2816. https://doi.org/10.1016/j.quascirev.2009.07.008.

Borchardt, S., Trauth, M.H., 2012. Remotely-Sensed Evapotranspiration estimates for an improved hydrological modeling of the early Holocene mega-lake Suguta, Northern Kenya Rift. Palaeogeogr. Palaeoclimatol. Palaeoecol. 361, 14–20.

Bosworth, W., Maurin, A., 1993. Structure, geochronology and tectonic significance of the Northern Suguta Valley (Gregory Rift), Kenya. J. Geol. Soc. Lond. 150 (4), 751–762. https://doi.org/10.1144/gsjgs.150.4.0751.

Brown, F.H., McDougall, I., 2011. Geochronology of the Turkana Depression of Northern Kenya and Southern Ethiopia. Evol. Anthropol. 20 (6), 217–227. https://doi.org/10.1002/evan.20318.

Casanova, J., Hillaire-Marcel, C., Page, N., Taieb, M., Vincens, A., 1988. Palaeohydrology and Late Quaternary Stratigraphy of Lacustrine Deposits in the Suguta Rift (Kenya). Comptes Rendus De Academie Des Sciences 307.

Castanier, S., Bernet-Rollande, M., Maurin, A., Perthuisot, J.-P., 1993. Effects of microbial activity on the hydrochemistry and sedimentology of Lake Logipi, Kenya. Hydrobiologia (the Hague) 267 (1–3), 99–112. https://doi.org/10.1007/BF00018793.

Cerling, T.E., Hay, R.L., 1986. An isotopic study of paleosol carbonates from Olduvai Gorge. Quat. Res. 25 (1), 63–78.

Chalié, F., Gasse, F., 2002. Late glacial-holocene diatom record of water chemistry and lake level change from the tropical east African Rift Lake Abiyata (Ethiopia). Palaeogeogr. Palaeoclimatol. Palaeoecol. 187 (3), 259–283. https://doi.org/10.1016/S0031-0182(02)00480-7.

Chorowicz, J., 2005. The East African Rift System. J. African Earth Sci. 43 (1), 379–410. https://doi.org/10.1016/j.jafrearsci.2005.07.019.

Clark, P.U., Archer, D., Pollard, D., Blum, J.D., Rial, J.A., Brovkin, V., Mix, A.C., Pisias, N. G., Roy, M., 2006. The Middle Pleistocene transition: characteristics, mechanisms, and implications for long-term changes in atmospheric pCO2. Quat. Sci. Rev. 25 (23–24), 3150–3184. https://doi.org/10.1016/j.quascirev.2006.07.008.

Clement, A.C., Hall, A., Broccoli, A.J., 2004. The importance of precessional signals in the tropical climate. Clim. Dyn. 22 (4), 327–341. https://doi.org/10.1007/s00382-003-0375-8.

Cocquyt, Christine, 1998. Diatoms from the Northern Basin of Lake Tanganyika. J. Cramer, Berlin.

Cohen, A.S., 1984. Effect of zoobenthic standing crop on laminae preservation in tropical lake sediment, Lake Turkana, East Africa. J. Paleontol, 499–510.

Davies, S.J., Lamb, H.F., Roberts, S.J., 2015. Micro-XRF core scanning in palaeolimnology: recent developments. In: Croudace, Ian W., Guy Rothwell, R. (Eds.), Micro-XRF Studies of Sediment Cores, Vol. 17. Springer, pp. 189–226.

Deino, A.L., Kingston, J.D., Glen, J.M., Edgar, R.K., Hill, A., 2006. Precessional forcing of Lacustrine sedimentation in the late Cenozoic Chemeron Basin, Central Kenya Rift, and calibration of the Gauss/Matuyama Boundary. Earth Planet. Sci. Lett. 247 (1), 41–60. https://doi.org/10.1016/j.epsl.2006.04.009.

Deino, A.L., Dommain, R., Keller, C.B., Potts, R., Behrensmeyer, A.K., Beverly, E.J., King, J., Heil, C.W., Stockhecke, M., Brown, E.T., Moerman, J., deMenocal, P., 2019a. Chronostratigraphic model of a high-resolution drill core record of the past million years from the Koora Basin, South Kenya Rift: overcoming the difficulties of variable sedimentation rate and hiatuses. Quat. Sci. Rev. 215 (74), 213–231. https://doi.org/10.1016/j.quascirev.2019.05.009.

Deino, Alan L., McBrearty, Sally, 2002. 40Ar/39Ar Dating of the Kapthurin Formation, Baringo, Kenya. J. Human Evol. 42 (1–2), 185–210. https://doi.org/10.1006/jhev.2001.0517.

Deino, A.L., Sier, M.J., Garello, D., Keller, B., Kingston, J., Scott, J., Dupont-Nivet, G., Cohen, A., 2019. Chronostratigraphy of the Baringo-Tugen-Barsemoi (HSPDP-BTB13-1A) Core – 40Ar/39Ar dating, magnetostratigraphy, tephrostratigraphy, sequence stratigraphy and Bayesian age modeling. In: 532. Palaeogeogr. Palaeoclimatol. Palaeoecol.. A high resolution, multi-proxy record of Pliocene hominin environments in the Kenya Rift Valley: Analysis of the Baringo-Tugen-Barsemoi (BTB) 109519.

deMenocal, P.B., 2004. African climate change and faunal evolution during the pliocene-pleistocene. Earth Planet. Sci. Lett. 220 (1), 3–24. https://doi.org/10.1016/S0012-821X(04)00003-2.

Dodson, R.G., 1963. Geological Map of the South Horr Area, , 60th ed.Vol. 1. Ministry of Commerce and Industry Mines and Geological Department of Kenya. 250,000.

Duesing, W., Kaboth-Bahr, S., Asrat, A., Cohen, A.S., Foerster, V., Lamb, H.F., Schaebitz, F., Trauth, M.H., Viehberg, F., 2021. Changes in the cyclicity and variability of the Eastern African paleoclimate over the last 620 Kyrs. Quat. Sci. Rev. 273, 107219 https://doi.org/10.1016/j.quascirev.2021.107219.

Dunkley, P.N., Srnith, M., Allen, D.J., Darling, W.G., 1993. The Geothermal Activity and Geology of the Northern Sector of the. Natural Environmental Research Council, Kenya Rift Valley.

Ebinger, C.J., Sleep, N.H., 1998. Cenozoic Magmatism throughout East Africa resulting from impact of a single plume. Nature 395 (6704), 788–791. https://doi.org/10.1038/27417.

Ebinger, C.J., Yemane, T., Harding, D.J., Tesfaye, S., Kelley, S., Rex, D.C., 2000. Rift Deflection, migration, and propagation; linkage of the Ethiopian and Eastern Rifts, Africa. Geol. Soc. Am. Bull. 112 (2), 163–176. https://doi.org/10.1130/0016-7606(2000)1122.0.CO;2.

Feibel, C.S., 2011. A geological history of the Turkana Basin. Evol. Anthropol. 20 (6), 206–216. https://doi.org/10.1002/evan.20331.

Fitzpatrick, R.W., Chittleborough, D.J., 2002. Titanium and Zirconium Minerals. Soil Mineral. Environ. Appl. 7, 667–690.
Foerster, V., Asrat, A., Ramsey, C.B., Brown, E.T., Chapot, M.S., Deino, A., Duesing, W., Grove, M., Hahn, A., Junginger, A., 2022. Pleistocene climate variability in Eastern Africa influenced hominin evolution. Nat. Geosci. 15 (10), 805–811.
Foerster, V., Deocampo, D.M., Asrat, A., Günter, C., Junginger, A., Krämer, K.H., Stroncik, N.A., Trauth, M.H., 2018. Towards an understanding of climate proxy formation in the Chew Bahir Basin, Southern Ethiopian Rift. Palaeogeogr. Palaeoclimatol. Palaeoecol. 501, 111–123. https://doi.org/10.1016/j.palaeo.2018.04.009.
Garcin, Y., Junginger, A., Melnick, D., Olago, D.O., Strecker, M.R., Trauth, M.H., 2009. Late pleistocene-holocene rise and collapse of Lake Suguta, Northern Kenya Rift. Quat. Sci. Rev. 28 (9), 911–925. https://doi.org/10.1016/j.quascirev.2008.12.006.
Garcin, Y., Melnick, D., Strecker, M.R., Olago, D., Tiercelin, J.-J., 2012. East African Mid-Holocene wet–dry transition recorded in palaeo-shorelines of Lake Turkana, Northern Kenya Rift. Earth Planet. Sci. Lett. 331–332, 322–334. https://doi.org/10.1016/j.epsl.2012.03.016.
Gasse, F., 1980. Les Diatomées Lacustres Plio-Pleistocenes Du Gadeb (Ethiopie): Systématique, Paléoécologique, Biostratigraphie. Rev. Algol. 3, 1–249.
Gasse, F., 1975. L'Évolution Des Lacs De L'Afar Central (Ethiopie Et T.F.A.I.) Du Plio-Pléistocene À L'Actuel. Reconstitution Des Paléomilieux Lacustres À Partir De L'Étude Des Diatomées. University of Paris, PhD.
Gasse, F., Juggins, S., Khelifa, L.B., 1995. Diatom-based transfer functions for inferring past hydrochemical characteristics of African lakes. Palaeogeogr. Palaeoclimatol. Palaeoecol. 117 (1), 31–54. https://doi.org/10.1016/0031-0182(94)00122-O.
Gasse, F., 1990. Tectonic and climatic controls on lake distribution and environments in Afar from miocene to present. In: Lacustrine Basin Exploration, pp. 19–41.
Gasse, F., 1986. East African Diatoms: Taxonomy, Ecological Distribution. J. Cramer, Berlin.
Genkal, S.I., 2009. New data on the morphology, taxonomy, ecology, and distribution of Stephanodiscus Agassizensis Håkansson Et Hickel (Bacillariophyta). Inland Water Biol. 2 (2), 113–126. https://doi.org/10.1134/S1995082909020035.
Hay, R.L., 1976. Geology of the Olduvai Gorge: A Study of Sedimentation in a Semiarid Basin. Univ. of California Press.
Head, Martin J., Gibbard, Philip L., 2005. Early-Middle Pleistocene Transitions: An Overview and Recommendation for the Defining Boundary. Geol. Soc. Spec. Publ 247 (1), 1–18. https://doi.org/10.1144/GSL.SP.2005.247.01.01.
Head, M.J., Pillans, B., Farquhar, S.A., 2008. The Early-Middle Pleistocene transition: characterization and proposed guide for the defining boundary. Episodes 31 (2), 255–259. https://doi.org/10.18814/epiiugs/2008/v31i2/014.
Hill, A., Curtis, G., Drake, R., 1986. Sedimentary Stratigraphy of the Tugen Hills, Baringo, Kenya. Geol. Soc. Spec. Publ. 25 (1), 285–295. https://doi.org/10.1144/GSL.SP.1986.025.01.23.
Isaac, G.L., Isaac, B., 1977. Olorgesailie: Archeological Studies of a Middle Pleistocene Lake Basin in Kenya. Univ. of Chicago Press.
Johnson, T.C., Werne, J.P., Brown, E.T., Abbott, A., Berke, M., Steinman, B.A., Halbur, J., Contreras, S., Grosshuesch, S., Deino, A., Lyons, R.P., Scholz, C.A., Schouten, S., Sinninghe Damste, J.S., 2016. A Progressively wetter climate in Southern East Africa over the past 1.3 million years. Nature 537 (7619), 220–224. https://doi.org/10.1038/nature19065.
Jolliffe, I.T., Cadima, J., 2016. Principal component analysis: a review and recent developments. Philos. Trans. A Math. Phys. Eng. Sci. 374 (2065), 20150202. https://doi.org/10.1098/rsta.2015.0202.
Joordens, J.C.A., Vonhof, H.B., Feibel, C.S., Lourens, L.J., Dupont-Nivet, G., van der Lubbe, J.H.J.L., Sier, M.J., Davies, G.R., Kroon, D., 2011. An astronomically-tuned climate framework for hominins in the Turkana Basin. Earth Planet. Sci. Lett. 307 (1), 1–8. https://doi.org/10.1016/j.epsl.2011.05.005.
Juggins, S., 2022. Rioja: Analysis of Quaternary Science Data. Vol. R package version 0.9-26.
Junginger, A., Kuebler, S., Rosca, C., Owen, R.B., Deino, A., Trauth, M.H., Vonhof, H., 2023. Mid-Pleistocene Volcano-Tectonic Fragmentation of the Turkana-Suguta Megalake. EGU Vienna April 24-29 2023.
Junginger, A., Roller, S., Olaka, L.A., Trauth, M.H., 2014. The effects of solar irradiation changes on the migration of the Congo air boundary and water levels of Paleo-Lake Suguta, Northern Kenya Rift, during the African Humid Period (15–5 Ka BP). Palaeogeogr. Palaeoclimatol. Palaeoecol. 396, 1–16. https://doi.org/10.1016/j.palaeo.2013.12.007.
Junginger, A., Trauth, M.H., 2013. Hydrological constraints of Paleo-Lake Suguta in the Northern Kenya Rift during the African Humid Period (15–5 Ka BP). Glob. Planet. Change. 111, 174–188. https://doi.org/10.1016/j.gloplacha.2013.09.005.
Kilham, P., Kilham, S.S., Hecky, R.E., 1986. Hypothesized resource relationships among African Planktonic Diatoms. Limnol. Oceanogr. 31 (6), 1169–1181. https://doi.org/10.4319/lo.1986.31.6.1169.
Kingston, J.D., Deino, A.L., Edgar, R.K., Hill, A., 2007. Astronomically forced climate change in the Kenyan Rift Valley 2.7–2.55 Ma: implications for the evolution of early hominin ecosystems. J. Hum. Evol. 53 (5), 487–503. https://doi.org/10.1016/j.jhevol.2006.12.007.
Kutzbach, J.E., Guanb, J., Hea, F., Cohen, A.S., Orlandd, I.J., Chend, G., 2020. African climate Response to Orbital and Glacial Forcing in 140,000-Y simulation with Implications for early Modern Human Environments. PNAS 117 (5), 2255–2264. https://doi.org/10.1073/pnas.1917673117.
Larrasoaña, J., Roberts, A., Rohling, E., Winklhofer, M., Wehausen, R., 2003. Three million years of monsoon variability over the Northern Sahara. Clim. Dyn. 21 (7), 689–698. https://doi.org/10.1007/s00382-003-0355-z.
Le Gall, B., Vétel, W., Morley, C.K., 2005. Inversion Tectonics during Continental Rifting: the Turkana Cenozoic Rifted Zone, Northern Kenya. Tectonics 24 (2). https://doi.org/10.1029/2004TC001637. TC2002-n/a.
Lee, J.-Y., Marti, K., Severinghaus, J.P., Kawamura, K., Yoo, H.-S., Lee, J.B., Kim, J.S., 2006. A redetermination of the isotopic abundances of atmospheric Ar. Geochim. Cosmochim. Acta 70, 4507–4512.
Lee, J., Kim, S., Khim, B.-K., 2020. A Paleoproductivity Shift in the Northwestern Bay of Bengal (IODP Site U1445) across the Mid-Pleistocene transition in Response to weakening of the Indian Summer Monsoon. Palaeogeogr. Palaeoclimatol. Palaeoecol. 560, 110018 https://doi.org/10.1016/j.palaeo.2020.110018.
Liutkus, C.M., Wright, J.D., Ashley, G.M., Sikes, N.E., 2005. Paleoenvironmental interpretation of lake-margin deposits using delta13C and delta18O results from early Pleistocene Carbonate Rhizoliths, Olduvai Gorge, Tanzania. Geol. 33 (5), 377–380. https://doi.org/10.1130/G21132.1.
Lowe, D.J., 2011. Tephrochronology and its application: a review. Quat. Geochronol. 6 (2), 107–153. https://doi.org/10.1016/j.quageo.2010.08.003.
Lupien, R.L., Russell, J.M., Pearson, E.J., Castañeda, I.S., Asrat, A., Foerster, V., Lamb, H. F., Roberts, H.M., Schabitz, F., Trauth, M.H., Beck, C.C., Feibel, C.S., Cohen, A.S., 2022. Orbital controls on Eastern African hydroclimate in the pleistocene. Sci. Rep. 12 (1), 3170. https://doi.org/10.1038/s41598-022-06826-z.
Makinouchi, T., Koyaguchi, T., Matsuda, T., Mitsushio, H., Ishida, S., 1984. In: Geology of the Nachola Area and the Samburu Hills, West of Baragoi, Northern Kenya. African Study Monographs. Supplementary Issue. 2, pp. 15–44.
Mannella, G., Giaccio, B., Zanchetta, G., Regattieri, E., Niespolo, E.M., Pereira, A., Renne, P.R., Nomade, S., Leicher, N., Perchiazzi, N., 2019. Palaeoenvironmental and palaeohydrological variability of mountain areas in the central mediterranean region: a 190 Ka-long chronicle from the independently Dated Fucino Palaeolake Record (Central Italy). Quat. Sci. Rev. 210, 190–210.
Martínez-Navarro, Bienvenido, Rabinovich, Rivka, 2011. The Fossil Bovidae (Artiodactyla, Mammalia) from Gesher Benot Ya'Aqov, Israel: Out of Africa during the Early-Middle Pleistocene Transition. J. Hum. Evol. 60 (4), 375–386. https://doi.org/10.1016/j.jhevol.2010.03.012.
Martin-Garcia, G., Sierro, F.J., Flores, J.A., Abrantes, F., 2018. Change in the North Atlantic Circulation Associated with the Mid-Pleistocene transition. Clim. Past 14 (11), 1639–1651. https://doi.org/10.5194/cp-14-1639-2018.
Maslin, M.A., Brierley, C.M., 2015. The role of orbital forcing in the Early Middle Pleistocene transition. Quat. Int. 389, 47–55. https://doi.org/10.1016/j.quaint.2015.01.047.
Maslin, M.A., Ridgwell, A.J., 2005. Mid-Pleistocene Revolution and the 'eccentricity Myth'. Geol. Soc. Spec. Publ. 247 (1), 19–34. https://doi.org/10.1144/GSL.SP.2005.247.01.02.
McClymont, E.L., Rosell-Melé, A., 2005. Links between the Onset of Modern Walker Circulation and the Mid-Pleistocene climate transition. Geol. 33 (5), 389–392. https://doi.org/10.1130/G21292.1.
McDougall, I., Harrison, T.M., 1999. Geochronology and Thermochronology by the 40Ar/39Ar Method. Oxford University Press on Demand, Oxford, New York.
McDougall, I., Brown, F.H., Vasconcelos, P.M., Cohen, B.E., Thiede, D.S., Buchanan, M.J., 2012. New single crystal 40Ar/39Ar ages improve time scale for deposition of the Omo Group, Omo-Turkana Basin, East Africa. J. Geol. Soc. Lond. 169 (2), 213–226. https://doi.org/10.1144/0016-76492010-188.
McLennan, S.M., 1993. Weathering and global denudation. J. Geol. 101 (2), 295–303. https://doi.org/10.1086/648222.
Melnick, D., Garcin, Y., Quinteros, J., Strecker, M.R., Olago, D., Tiercelin, J.-J., 2012. Steady rifting in Northern Kenya inferred from deformed Holocene Lake Shorelines of the Suguta and Turkana basins. Earth Planet. Sci. Lett. 331–332, 335–346. https://doi.org/10.1016/j.epsl.2012.03.007.
Meyer, I., Van Daele, M., Tanghe, N., De Batist, M., Verschuren, D., 2020. Reconstructing East African monsoon variability from grain-size distributions: end-member modeling and source attribution of diatom-rich sediments from Lake Chala. Quat. Sci. Rev. 247, 106574 https://doi.org/10.1016/j.quascirev.2020.106574.
Min, K.W., Mundil, R., Renne, P.R., Ludwig, K.R., 2000. A test for systematic errors in Ar-40/Ar-39 geochronology through comparison with U/Pb analysis of a 1.1-Ga rhyolite. Geochim. Cosmochim. Acta 64 (1), 73–98.
Morley, C.K., Wescott, W.A., Stone, D.M., Harper, R.M., Wigger, S.T., Karanja, F.M., 1992. Tectonic evolution of the Northern Kenyan Rift. J. Geol. Soc. Lond. 149 (3), 333–348. https://doi.org/10.1144/gsjgs.149.3.0333.
Mosley, P.N., 1993. Geological evolution of the Late Proterozoic "Mozambique Belt" of Kenya. Tectonophysics 221 (2), 223–250.
Mudelsee, M., Stattegger, K., 1997. Exploring the structure of the Mid-Pleistocene revolution with advanced methods of time-series analysis. Geol. Rundsch. 86 (2), 499–511. https://doi.org/10.1007/s005310050157.
Mudelsee, M., Schulz, M., 1997. The Mid-Pleistocene climate transition: onset of 100 Ka cycle lags ice volume build-up by 280 Ka. Earth Planet. Sci. Lett. 151 (1), 117–123. https://doi.org/10.1016/S0012-821X(97)00114-3.
Muiruri, Veronica, Owen, R.B., Potts, Richard, Deino, Alan L., Behrensmeyer, Anna K., Riedl, Simon, Nathan Rabideaux, T.K., Lowenstein, K., Leet, M., Sier, A., Cohen, D., Deocampo, C.J., Campisano, A.Billingsley, Mbuthia, A., 2021a. Quaternary diatoms and palaeoenvironments of the Koora Plain, Southern Kenya Rift. Quat. Sci. Rev. 267, 107106 https://doi.org/10.1016/j.quascirev.2021.107106.
Muiruri, V.M., Owen, R.B., Lowenstein, T.K., Renaut, R.W., Marchant, R., Rucina, S.M., Cohen, A., Deino, A.L., Sier, M.J., Luo, S., Leet, K., Campisano, C., Rabideaux, N.M., Deocampo, D., Shen, C.-C., Mbuthia, A., Davis, B.C., Aldossari, W., Wang, C., 2021b. A million year vegetation history and palaeoenvironmental record from the Lake Magadi Basin, Kenya Rift Valley. Palaeogeogr. Palaeoclimatol. Palaeoecol. 567, 110247 https://doi.org/10.1016/j.palaeo.2021.110247.

Nesbitt, H.W., Young, G.M., 1982. Early proterozoic climates and plate motions inferred from major element chemistry of Lutites. Nature 299 (5885), 715–717. https://doi.org/10.1038/299715a0.
Nicholson, Sharon E., 1996. A Review of Climate Dynamics and Climate Variability in Eastern Africa. In: Johnson, Thomas C., Odada, Eric O., Whittaker, Katherine T. (Eds.), the Limnology, Climatology and Paleoclimatology of the East African Lakes., Amsterdam, the Netherlands, 1996. Gordon and Breach Science Publishers, pp. 25–56.
Nicholson, S.L., Pike, A.W.G., Hosfield, R., Roberts, N., Sahy, D., Woodhead, J., Cheng, H., Edwards, R.L., Affolter, S., Leuenberger, M., Burns, S.J., Matter, A., Fleitmann, D., 2020. Pluvial periods in Southern Arabia over the last 1.1 million-years. Quat. Sci. Rev. 229, 106112 https://doi.org/10.1016/j.quascirev.2019.106112.
Nicholson, S.E., 2017. Climate and climatic variability of rainfall over Eastern Africa. Rev. Geophys. 55 (3), 590–635. https://doi.org/10.1002/2016RG000544.
Niespolo, E.M., Rutte, D., Deino, A.L., Renne, P.R., 2017. Intercalibration and age of the Alder Creek sanidine Ar-40/Ar-39 standard. Quat. Geochronol. 39, 205–213.
Nyenzi, B.S., Kiangi, P.M.R., Rao, N.N.P., 1981. Evaporation Values in East Africa. Arch. Meteorol. Geophys. Bioclimatol. Ser. B 29 (1–2), 37–55. https://doi.org/10.1007/BF02278189.
Ochieng, J.O., 1988. Geology of the Loiyangalani. Area 1 (250), 000.
Ojany, F., Ogendo, R., 1973. Kenya; A Study in Physical and Human Geography. Longman Publishers, Nairobi, Kenya.
Olaka, L., Odada, E., Trauth, M., Olago, D., 2010. The sensitivity of East African rift lakes to climate fluctuations. J. Paleolimnol. 44 (2), 629–644. https://doi.org/10.1007/s10933-010-9442-4.
O'Sullivan, P.E., 1983. Annually-laminated lake sediments and the study of quaternary environmental changes — a review. Quat. Sci. Rev. 1 (4), 245–313. https://doi.org/10.1016/0277-3791(83)90008-2.
Owen, R.B., Crossley, R., 1992. Spatial and temporal distribution of diatoms in sediments of Lake Malawi, Central Africa, and ecological implications. J. Paleolimnol. 7 (1) https://doi.org/10.1007/BF00197031.
Owen, R.B., Potts, R., 2009. Reply to the Comment on "Diatomaceous Sediments and Environmental Change in the Pleistocene Olorgesailie Formation, Southern Kenya Rift Valley. Palaeogeography, Palaeoclimatology, Palaeoecology 282, 147–148.
Owen, R.B., Lee, R.K.L., Renaut, R., 2012. Early pleistocene lacustrine sedimentation and diatom stratigraphy at Munya Wa Gicheru, Southern Kenya Rift Valley. Palaeogeogr. Palaeoclimatol. Palaeoecol. 331–332, 60–74. https://doi.org/10.1016/j.palaeo.2012.02.033.
Owen, R.B., Renaut, R.W., Behrensmeyer, A.K., Potts, R., 2014. Quaternary geochemical stratigraphy of the Kedong-Olorgesailie section of the Southern Kenya Rift Valley. Palaeogeogr. Palaeoclimatol. Palaeoecol. 396, 194–212. https://doi.org/10.1016/j.palaeo.2014.01.011.
Owen, R.B., Muiruri, V., Lowenstein, T., Renaut, R., Rabideaux, N., Luo, S., Deino, A., Sier, M.J., Dupont-Nivet, G., McNulty, E.P., Leet, K., Cohen, A., Campisano, C., Deocampo, D., Shen, C.-C., Billingsley, A., Mbuthia, A., 2018a. Progressive aridification in East Africa over the last half million years and implications for human evolution. PNAS 115 (44), 11174–11179. https://doi.org/10.1073/pnas.1801357115.
Owen, R. Bernhart, Renaut, Robin W., Muiruri, Veronica M., Rabideaux, Nathan M., Lowenstein, Tim K., McNulty, Emma P., Leet, Kennie, et al., 2019. Quaternary History of the Lake Magadi Basin, Southern Kenya Rift: Tectonic and Climatic Controls. Palaeogeogr. Palaeoclimatol. Palaeoecol. 518, 97–118. https://doi.org/10.1016/j.palaeo.2019.01.017.
Owen, R.Bernhart, Renaut, R.W., 2000. Miocene and pliocene diatomaceous lacustrine sediments of the Tugen Hils, Baringo District, Central Kenya Rift. In: Gierlowski-Kordesch, E.H., Kelts, K.R. (Eds.), Lake Basins through Space and Time, pp. 465–472. AAPG Studies in Geology.
Owen, R.B., Renaut, R.W., Lowenstein, T.K., Brasier, A., 2018b. Spatial and temporal geochemical variability in lacustrine sedimentation in the East African Rift System: evidence from the Kenya Rift and regional analyses. Sedimentology 65 (5), 1697–1730. https://doi.org/10.1111/sed.12443.
Paillard, D., 1998. The timing of Pleistocene Glaciations from a simple multiple-state climate model. Nature 391 (6665), 378–381.
Pik, R., Marty, B., Carignan, J., Yirgu, G., Ayalew, T., 2008. Timing of East African rift development in Southern Ethiopia; implication for mantle plume activity and evolution of topography. Geology 36 (2), 167–170. https://doi.org/10.1130/G24233A.1.
Pilskaln, C.H., Johnson, T.C., 1991. Seasonal signals in Lake Malawi sediments. Limnol. Oceanogr. 36 (3), 544–557. https://doi.org/10.4319/lo.1991.36.3.0544.
Pisias, N.G., Moore, T.C., 1981. The evolution of pleistocene climate: a time series approach. Earth Planet. Sci. Lett. 52 (2), 450–458. https://doi.org/10.1016/0012-821X(81)90197-7.
Potts, R., Behrensmeyer, A.K., Ditchfield, P., 1999. Paleolandscape variation and Early Pleistocene hominid activities: members 1 and 7, Olorgesailie Formation, Kenya. J. Hum. Evol. 37 (5), 747–788. https://doi.org/10.1006/jhev.1999.0344.
Potts, R., Behrensmeyer, A.K., Faith, J.T., Tryon, C.A., Brooks, A.S., Yellen, J.E., Deino, A. L., Kinyanjui, R., Clark, J.B., Haradon, C.M., Levin, N.E., Meijer, H.J.M., Veatch, E. G., Owen, R.B., Renaut, R.W., 2018. Environmental dynamics during the onset of the Middle Stone Age in Eastern Africa. Science 360 (6384), 86. https://doi.org/10.1126/science.aao2200.
Potts, R., Dommain, R., Moerman, J.W., Behrensmeyer, A.K., Deino, A.L., Riedl, S., Beverly, E.J., Brown, E.T., Deocampo, D., Kinyanjui, R., Lupien, R., Owen, R.B., Rabideaux, N., Russell, J.R., Stockhecke, M., deMenocal, P., Faith, J.T., Garcin, Y., Noren, A., Scott, J.J., Wastern, D., Bright, J., Clark, J.B., Cohen, A.S., Keller, C.B., King, J., Levin, N.E., Shannon, K.B., Muiruri, V., Renaut, R.W., Rucina, S.M., Uno, K., 2020. Increased ecological resource variability during a critical transition in hominin evolution. Sci. Adv. 6 (43), eabc8975. https://doi.org/10.1126/sciadv.abc8975.
Purcell, P.G., 2018. Re-imagining and re-imaging the development of the East African Rift. Pet. Geosci. 24 (1), 21–40. https://doi.org/10.1144/petgeo2017-036.
Renaut, R.W., Ego, J., Tiercelin, J.J., Le Turdu, C., 1999. Saline, Alkaline Palaeolakes of the Tugen Hills-Kerio Valley Region, Kenya Rift Valley. In: *Late Cenozoic Environments and Hominid Evolution: A Tribute to Bill Bishop.Geological.* Society, London, pp. 41–58.
Renaut, R.W., Owen, R.B., Lowenstein, T.K., De Cort, G., Mcnulty, E., Scott, J.J., Mbuthia, A., 2021. The role of hydrothermal fluids in sedimentation in saline alkaline lakes: evidence from Nasikie Engida, Kenya Rift Valley. Sedimentology 68 (1), 108–134.
Rossignol-Strick, M., 1984. Mediterranean quaternary sapropels, an immediate response of the African monsoon to variation of insolation. Palaeogeogr. Palaeoclimatol. Palaeoecol. 49 (3), 237–263. https://doi.org/10.1016/0031-0182(85)90056-2.
Ryves, D.B., Anderson, N.J., Flower, R.J., Rippey, B., 2013. Diatom taphonomy and silica cycling in two freshwater lakes and their implications for inferring past lake productivity. J. Paleolimnol. 49 (3), 411–430. https://doi.org/10.1007/s10933-013-9694-x.
Saneyoshi, M., Nakayama, K., Sakai, T., Sawada, Y., Ishida, H., 2006. Half graben filling processes in the early phase of continental rifting: the Miocene Namurungule Formation of the Kenya Rift. Sediment. Geol. 186 (1), 111–131. https://doi.org/10.1016/j.sedgeo.2005.11.012.
Shackleton, N.J., Opdyke, N.D., 1977. Oxygen-isotope and paleomagnetic stratigraphy of Pacific Core V28–239 late Pliocene to latest Pleistocene. Deep-Sea Res. 24 (4), 449–464. https://doi.org/10.1016/0146-6291(77)90420-9.
Spaulding, S.A., Bishop, I.W., Edlund, M.B., Lee, S., Furey, P., Jovanovska, E., Potapova, M., 2022. Diatoms of North America. https://diatoms.org/species.
Stanistreet, I.G., Doyle, C., Hughes, T., Rushworth, E.D., Stollhofen, H., Toth, N., Schick, K., Njau, J.K., 2020. Changing depocentre environments of Palaeolake Olduvai and carbonates as marker horizons for hiatuses and lake-level extremes. Palaeogeogr. Palaeoclimatol. Palaeoecol. 560, 110032 https://doi.org/10.1016/j.palaeo.2020.110032.
Sturchio, N.C., Dunkley, P.N., Smith, M., 1993. Climate-driven variations in geothermal activity in the Northern Kenya Rift Valley. Nature 362 (6417), 233–234. https://doi.org/10.1038/362233a0.
Sun, Y., Clemens, S.C., An, Z., Yu, Z., 2006. Astronomical timescale and palaeoclimatic implication of stacked 3.6-Myr monsoon records from the Chinese Loess Plateau. Quat. Sci. Rev. 25 (1), 33–48. https://doi.org/10.1016/j.quascirev.2005.07.005.
Taylor, J.C., Harding, W.R., Archibald, C.G.M., 2007. An Illustrated Guide to some Common Diatom Species from South Africa. Water Research Commission, Pretoria, South Africa.
ter Braak, C., Looman, C., 1986. Weighted averaging, logistic regression and the Gaussian response model. Vegetation 65 (1), 3-–11. https://doi.org/10.1007/BF00032121.
Tierney, J.E., Lewis, S.C., Cook, B.I., Legrande, A.N., Schmidt, G.A., 2011. Model, proxy and isotopic perspectives on the East African humid period. Earth Planet. Sci. Lett. 307 (1), 103–112. https://doi.org/10.1016/j.epsl.2011.04.038.
Trauth, M.H., Larrasoana, J.C., Mudelsee, M., 2009. Trends, rhythms and events in plio-pleistocene African climate. In: Katlenburg-Lindau: Katlenburg-Lindau, Vol. 11. Copernicus GmbH on behalf of the European Geosciences Union (EGU), Germany.
Trauth, M.H., 2014. A new probabilistic technique to build an age model for complex stratigraphic sequences. Quat. Geochronol. 22, 65–71. https://doi.org/10.1016/j.quageo.2014.03.001.
Trauth, M.H., Bergner, A.G.N., Foerster, V., Junginger, A., Maslin, M.A., Schaebitz, F., 2015. Episodes of environmental stability versus instability in late Cenozoic Lake records of Eastern Africa. J. Hum. Evol. 87, 21–31. https://doi.org/10.1016/j.jhevol.2015.03.011.
Trauth, M.H., Maslin, M.A., Deino, A.L., Junginger, A., Lesoloyia, M., Odada, E.O., Olago, D.O., Olaka, L.A., Strecker, M.R., Tiedemann, R., 2010. Human evolution in a variable environment: the amplifier lakes of Eastern Africa. Quat. Sci. Rev. 29 (23), 2981–2988. https://doi.org/10.1016/j.quascirev.2010.07.007.
Trauth, M.H., Maslin, M.A., Deino, A.L., Strecker, M.R., Bergner, A.G.N., Dühnforth, M., 2007. High- and low-latitude forcing of Plio-Pleistocene East African climate and human evolution. J. Hum. Evol. 53 (5), 475–486. https://doi.org/10.1016/j.jhevol.2006.12.009.
Trauth, M.H., Maslin, M.A., Deino, A., Strecker, M.R., 2005. Late Cenozoic Moisture history of East Africa. Science 309 (5743), 2051–2053. https://doi.org/10.1126/science.1112964.
Truckle, P.H., 1976. Geology and late Cainozoic Lake sediments of the Suguta Trough, Kenya. Nature 263 (5576), 380–383. https://doi.org/10.1038/263380a0.
Truckle, P.H., 1977. The Geology of the Area to the South of Lokori. Kenya University of Leicester (United Kingdom), South Turkana.
Van Kekem, A.J., 1986. Reconnaissance Soil Map of the Mount Kulala-Marsabit Area, , 12th ed.Vol. 1. Kenya Soil Survey, Ministry of Agriculture, and UNESCO Integrated Project of Arid Lands (IPAL).
van Kolfschoten, Thijs, Markova, Anastasia K., 2005. Response of the European Mammalian Fauna to the Mid-Pleistocene Transition. Geol. Soc. Spec. Publ. 247 (1), 221–229. https://doi.org/10.1144/GSL.SP.2005.247.01.12.
Vetel, W., Le Gall, B., 2006. Dynamics of prolonged continental extension in Magmatic Rifts: the Turkana Rift Case Study (North Kenya). Geol. Soc. Spec. Publ. 259 (1), 209–233. https://doi.org/10.1144/GSL.SP.2006.259.01.17.
Vrba, E., 1996. The Fossil Record of African Antelopes (Mammalia, Bovidae) in Relation to Human Evolution and Paleoclimate." Paleoclimate and Evolution, with Emphasis on. Human Origins 385–424.

Vuille, M., Werner, M., Bradley, R.S., Chan, R.Y., Keimig, F., 2005. Stable Isotopes in East African Precipitation Record Indian Ocean Zonal Mode. Geophys. Res. Lett. 32 (21) https://doi.org/10.1029/2005GL023876. L21705-n/a.

Weaver, S.D., 1977. The Quaternary Caldera Volcano Emuruangogolak, Kenya Rift, and the petrology of a Bimodal Ferrobasalt-Pantelleritic Trachyte Association. Bull. Volcanol. 40 (4), 209–230. https://doi.org/10.1007/BF02597564.

Xue, L., Gani, N.D., Abdelsalam, M.G., 2019. Drainage Incision, Tectonic Uplift, Magmatic activity, and Paleo-Environmental changes in the Kenya Rift, East African Rift System: a Morpho-Tectonic analysis. Geomorphology 345, 106839. https://doi.org/10.1016/j.geomorph.2019.106839.

Yost, C.L., Lupien, R.L., Beck, C., Feibel, C.S., Archer, S.R., Cohen, A.S., 2021. Orbital Influence on Precipitation, Fire, and Grass Community Composition from 1.87 to 1.38 Ma in the Turkana Basin, Kenya. Front. Earth Sci. 9 https://doi.org/10.3389/feart.2021.568646.